

Ferromagnetic Properties of Mixed Spinel Ferrites: Co-Zn and Ni-Zn-Mn

K. Praveena^{1,2,a*}, K. Sadhana^{3,b} and H.S. Virk^{4,c}

¹Materials Research Centre, Indian Institute of Science, Bangalore -560012, India.

²Department of Physics, Eternal University, Baru Sahib-173101, Himachal Pradesh, India

³Department of Physics, University College of Science, Osmania University, Saifabad, Hyderabad – 500 004, India

⁴Professor Emeritus, Eternal University, Baru Sahib, Himachal Pradesh, India

^apraveenaou@gmail.com (*corresponding author), ^bsadhanaphysics@gmail.com,

^chardevsingh.virk@gmail.com

Keywords: Spinel Ferrites, Magnetic Properties, Saturation Magnetization, Zero Field Cooling, Blocking Temperature, Permeability, Q-factor, DC-bias-superposition.

Abstract. Among the spinel ferrites, Zn-substituted mixed ferrites are useful for low and high frequency applications, generally for power transformers, power inductors, microwave devices, read and write heads for high speed digital tape, etc. because of their high resistivity, low losses, mechanical hardness, high Curie temperature and chemical stability. Cobalt zinc ferrite is one of the promising soft ferrite used in electronic devices such as transformer cores, electric motors and generators. Zn substituted mixed ferrites (Co-Zn) are chosen due to their high sensitivity of magnetization to temperature for some applications like self-controlled hyperthermia. Our aim is to investigate ferromagnetic properties of mixed spinel ferrites, Co-Zn and Ni-Zn-Mn, and effect of Zn substitution on properties of these spinel ferrites.

Nanocrystalline $\text{Co}_{1-x}\text{Zn}_x\text{Fe}_2\text{O}_4$ ($0 \leq x \leq 1$) powders were synthesized using microwave hydrothermal method. The synthesized powders were characterized by XRD, TEM and FTIR. The average particle size was obtained from TEM and it is found to be 17 nm. Zero field cooled (ZFC) and Field cooled (FC) measurements reveal that samples with $0.6 \leq x \leq 1$ have super-paramagnetic behaviour at room temperature, which confirms weak interaction between magnetic particles. The blocking temperatures obtained from ZFC-FC curves decreases as Zn concentration increases. Lower reduced remnant magnetization (M_r/M_s) values ($x < 0.5$) suggest that all the samples have uniaxial anisotropy.

$\text{Ni}_{0.4}\text{Zn}_{0.2}\text{Mn}_{0.4}\text{Fe}_2\text{O}_4$ nanopowders were synthesized via auto-combustion method. The as-synthesized powders were characterized using X-ray diffraction (XRD) and thermo-gravimetric-differential thermal analysis (TG-DTA), the powders were sintered at different temperatures 400°C, 500°C, 600°C and 700°C/4hrs using conventional sintering method. The sintered samples were characterized by XRD and transmission electron microscope (TEM). The bulk densities of the samples were increased with an increase of sintering temperature. The grain sizes of all the samples vary between 18 nm to 30 nm. The hysteresis loops show high saturation magnetization and low coercivity, which indicates that it is a soft material. The incremental permeability (permeability with magnetic field superposition) was influenced by both ΔM and H_c .

Contents of Paper

1. Introduction to Mixed Spinel Ferrites
2. Experimental
 - 2.1. Synthesis of Co-Zn ferrites
3. Results and discussions
 - 3.1. Structural and morphological studies
 - 3.2. Transmission electron microscope (TEM) analysis
 - 3.3. Fourier transform infrared spectroscopy (FTIR)
 - 3.4. Room temperature M-H loops

- 3.5. Y-K angles
- 3.6. M-T analysis
- 4. Synthesis of $\text{Ni}_{0.4}\text{Zn}_{0.2}\text{Mn}_{0.4}\text{Fe}_2\text{O}_4$
- 5. Results and Discussion
 - 5.1. Thermo-gravimetric analysis
 - 5.2. X-ray diffraction and Rietveld refinement
 - 5.3. Transmission Electron Microscopy
 - 5.4. Room temperature M-H loops
 - 5.5. Magnetic field dependent permeability
 - 5.6. Magnetic field dependent quality factor
- 6. Conclusions
- References

1. Introduction to Mixed Spinel Ferrites

Ferrites have the general formula $(\text{M}_{1-x}\text{Fe}_x)[\text{M}_x\text{Fe}_{2-x}]\text{O}_4$. The divalent metal element M (Mg, Zn, Mn, Fe, Co, Ni, or mixture of them) can occupy either tetrahedral eight (A) or sixteen octahedral [B] sites of a cubic mineral spinel (MgAl_2O_4) structure as depicted by the parentheses or brackets, respectively. For example the structural formula of Co-ferrite is usually written as $(\text{Co}_{1-x}\text{Fe}_x)[\text{Mg}_x\text{Fe}_{2-x}]\text{O}_4$, where x represents the degree of inversion (defined as the fraction of (A) sites occupied by Fe^{3+} cations). Depending on distribution of cations in (A) and [B] sites, ferrites may exist in two extreme states, normal ($x = 0$) and inverse ($x = 1$) or in an intermediate mixed state [1].

Among these materials, spinel ferrite nanoparticles have special importance. They show various magnetic properties depending on the composition and cation distribution. Various cations can be placed in A site and B site to tune its magnetic properties. Depending on A site and B site cations, it can exhibit ferrimagnetic, antiferromagnetic, spin (cluster) glass, and paramagnetic behaviour.

Nanosized ferrites may have extraordinary electric and magnetic properties that are comparatively different from microstructured materials, tailoring them to modern technologies, as well as providing novel applications such as ferrofluids [2], magnetic drug delivery [3], high density information storage [4], photocatalysis [5], gas sensors [6], etc.

Among those spinel ferrites we are interested in Zn substituted mixed ferrites are useful for low and high frequency applications generally for power transformers, power inductors, microwave devices, read and write heads for high speed digital tape, etc. because of their high resistivity, low losses, mechanical hardness, high Curie temperature and chemical stability [7-12].

CoFe_2O_4 has attracted considerable interest because of its large magnetic multi-axial anisotropy, high saturation magnetization, high Curie temperature and extraordinary chemical stability [13-16]. CoFe_2O_4 is predominantly an inverse spinel oxide with Co^{2+} ions mainly on B sites and Fe^{3+} ions distributed, almost equally, between A and B sites [17]. Cobalt ferrite is ferrimagnetic below 790 K (T_N) which suggests that the magnetic interactions in this ferrite are very strong. When Co^{2+} is replaced by Zn^{2+} in $\text{Co}_{1-x}\text{Zn}_x\text{Fe}_2\text{O}_4$, Zn^{2+} preferentially occupies the tetrahedral site and the Fe^{3+} ions are displaced to the octahedral sites. Thus, with increasing x , the $\text{Fe}_A\text{--O--Fe}_B$ interaction becomes weak and T_N is expected to decrease. ZnFe_2O_4 is a normal spinel, i.e., $\text{Zn}_A[\text{Fe}_2]_B\text{O}_4$, and it is not ferrimagnetic, but antiferromagnetic due to $\text{Fe}_B\text{--Fe}_B$ interactions only. T_N of ZnFe_2O_4 is very small, 9 K [18]. The absence of magnetic ions on the A site does not permit the antiferromagnetic A–O–B interaction and hence the magnetic interaction in this ferrite is only on the octahedral (B) site. Now as the overall interaction in a ferrite is antiferromagnetic, the only magnetic interaction in ZnFe_2O_4 , i.e., $\text{Fe}_B\text{--Fe}_B$ is antiferromagnetic [19].

Cobalt zinc ferrite is one of the promising soft ferrite used in electronic devices such as transformer cores, electric motors and generators. Cobalt ferrite nanoparticles are suitable for the isolation and refining of genomic DNA, the parting of polymerase chain reaction ready DNA [20, 21] and especially in hyperthermia treatment. Variation in the concentration of the third metal ion like Zn in Co ferrite can easily alter the distribution of Fe^{3+} ion [22]. Zn substituted mixed ferrites (Co-Zn) are chosen due to their high sensitivity of magnetization to temperature for some applications like self-controlled hyperthermia [23-25].

Till now, low-temperature-fired Ni-Cu-Zn ferrites are the most important materials subjected to study the DC-bias-superposition characteristics [26-28] due to their relatively low sintering temperature, high resistivity and good magnetic properties in the high frequency range [29, 30]. But these investigations were mainly focused how to lower sintering temperature of the NiCuZn ferrites by adding various sintering aids or changing the preparation process, improving the electromagnetic properties [31-37] but there are no reports present on pure NiCuZn ferrite which was studied for DC bias superposition. And, moreover, they are the most important soft ferrites used in multilayer chip inductors (MLCIs) and relevant inductive devices [38-40, 29]. In this work, we chose Mn element to replace Cu element in the NiCuZn ferrites, and investigated the effects of 'Mn' on the magnetic properties, especially DC-bias-superposition characteristic.

Studies on spinel ferrites synthesis methods have led to the development of different chemical synthesis techniques, which have a common feature that all reagents are mixed in atomic or molecular level. Most popular methods of bottom-up synthesis approach mentioned above are co-precipitation [41], sol-gel method [42], microemulsion method [43], hydrothermal [44], spray pyrolysis [45], reverse micelle [46], precursor method [47], etc. Complex schedules and low production rate are common problems of these wet-chemical methods [48].

The main advantages of this process over conventional-hydrothermal process are: (a) the rapid heating to treatment temperature saves time and energy, (b) the kinetics of the reaction are enhanced by one to two orders of magnitude, (c) lead to the formation of novel phases, and (d) lead to selective crystallization. Praveena et al. [49-52] have used the microwave hydrothermal (M-H) method to prepare nano-sized powders of various ferrites with large surface area.

Sol-gel auto-combustion synthesis method (also called low-temperature self-combustion, auto-ignition or self-propagation, as well as gel-thermal decomposition), where the chemical sol-gel and combustion process are combined, has shown great potential in the preparation of spinel type ferrite nanomaterials. Generally, this method can be considered as solution combustion technique [53].

1. Experimental

2.1. Synthesis of $\text{Co}_{1-x}\text{Zn}_x\text{Fe}_2\text{O}_4$ Ferrites: Nanocrystalline powders with compositions $\text{Co}_{1-x}\text{Zn}_x\text{Fe}_2\text{O}_4$ ($0 \leq x \leq 1$) were prepared using microwave hydrothermal route. High purity (sigma, 99.99%) of cobalt nitrate [$\text{Co}(\text{NO}_3)_2 \cdot 6\text{H}_2\text{O}$], zinc nitrate [$\text{Zn}(\text{NO}_3)_2 \cdot 6\text{H}_2\text{O}$] and iron nitrate [$\text{Fe}(\text{NO}_3)_3 \cdot 9\text{H}_2\text{O}$] were dissolved in double de-ionized water. An aqueous NaOH was added dropwise to the solution until pH (~13) was obtained. The mixture was then transferred into Teflon lined vessel and kept in microwave digestion system (Model MDS-2000, CEM Corp., Mathews, NC). This system uses 2.45 GHz microwaves and can operate at 0-100% full power ($1200 \pm 50\text{W}$). The system is controlled by pressure and can attain maximum pressure of 200 psi, which is equivalent to 194°C . The time, pressure and powder were computer controlled. The products obtained were filtered and then washed repeatedly with de-ionized water, followed by freeze drying overnight. The prepared powders were weighed and the percentage yields were calculated from the actual weight of the salts taken and the amount that was actually crystallized. The particle sizes of as-synthesized powders were estimated by Transmission Electron Microscope (TEM, JEOL). FTIR

spectra's were taken on Bruker Tensor 27 model from 4000 to 400 cm^{-1} . The samples were characterized by Phillips PANalytical X'pert powder X-ray diffraction (XRD) with Cu-K α ($\lambda=1.5406\text{\AA}$) radiation. The lattice constant (a) for the cubic crystal system was calculated using the equation $a = d\sqrt{h^2 + k^2 + l^2}$ where (h k l) are the Miller indices of the diffraction peak, and 'd' is the inter-planar spacing. The average crystallite size was calculated from Scherer formula $D_m = K\lambda / \beta \cos \theta$ where K is a constant, λ radiation wavelength, β is full width at half maxima (FWHM) and θ is the diffraction angle. The distance between magnetic ions, hopping lengths in octahedral sites and tetrahedral sites is given by the following relation: $L_A = a\frac{\sqrt{3}}{4}$; $L_B = a\frac{\sqrt{2}}{4}$ [54]. Magnetic measurements were obtained from a super conducting quantum interference device (SQUID) at room temperature (400 K).

3. Results and Discussions

3.1. Structural and morphological studies: Fig. 1 shows powder X-ray diffraction patterns of as-synthesized nanopowders. It shows single-phase cubic spinel structure, without any impurity phases. It is interesting to observe that as Zn concentration is increasing the diffraction peaks become broader indicating the nanosize of the crystals with space group symmetry, $fd\bar{3}m$ [55]. The experimental values of lattice constants are compared with the standard JCPDS-ICDD Cards, for Co ferrite (22-1086 ICDD) and for Zn ferrite (89-1009 ICDD).

Using XRD results, the average crystallite size of the samples was calculated as given in Table 1. When the crystallite size drops from bulk to nanosize, the cation distributions as well as the magnetic properties of the compounds would be altered drastically. As the Zn^{2+} concentration increases crystallite size decreased from 20 to 15 nm, this result conveys that the introduction of Zn in CoFe_2O_4 obstructs the crystal growth, which is based on the entropy stabilization which forms disorder in the spinel structure reported by Sharifi and Shokrollahi [56]. The formation of free energy will be comparable to enthalpy of formation for normal spinels and somewhat more negative for spinels with intermediate or inverse cation distributions [57]. As expected the introduction of zinc in the system, more heat will be liberated, decreasing the molecular concentration at the crystal surface and there by obstructing the crystal growth [58, 41]. It is interesting to note that Zn^{2+} ions in the spinel structure have a very strong preference for tetrahedral sites and Co^{2+} ions have a similar strong preference for octahedral sites. Also Fe^{3+} ions have a stronger preference for the tetrahedral sites as compared to the octahedral sites. As Zn is introduced in the system, it forces Fe^{3+} to occupy octahedral sites and the situation becomes less favourable. The decrease in particle size by increase in Zn content may be explained by the electronic configuration of Co^{2+} ($3d^7$) and its more tendency to interact with ligands and oxygen anions, as compared to Zn^{2+} ($3d^{10}$), which has a complete electronic configuration. The lack of 'd' electron is important because it is very weak in covalent interaction and there is a tendency towards extension between Zn^{2+} and ligand. Furthermore, it is reported by some researchers [59] that the smaller particle sizes of the samples doped with Zn ions are due to the lower bond energy of $\text{Zn}^{2+}-\text{O}^{2-}$ (159 kJ/mol) as compared with that of $\text{Co}^{2+}-\text{O}^{2-}$ (384kJ/mol).

The lattice constants of the present samples vary from 8.388 to 8.44 \AA and are given in Table 1. It is observed that lattice constant ' a ' increases as zinc content (x) increases. This variation can be explained on the basis of difference in ionic radii of the substituted ions. The ionic radii of Zn^{2+} (0.82 \AA) [60] is larger than that of Co^{2+} (0.78 \AA) [61] ions. In the present system Zn^{2+} ions are substituted in place of Co^{2+} ions and hence lattice constant increases with Zn content (x).

The distance between magnetic ions at tetrahedral A (L_A) and octahedral B (L_B) sites was calculated and is shown in Fig. 2. Both L_A and L_B increase with Zn. This may be attributed to the increase in lattice constant of the samples.

Using the cation distribution data the mean ionic radius of tetrahedral (A) site (r_A) and octahedral [B] site (r_B) was calculated. It is observed from Fig. 3 that r_A increases and r_B decreases with zinc substitution. The increase in r_A is due to the replacement of Fe^{3+} ions at the tetrahedral A-site by the larger radius Zn^{2+} ions. The decrease in r_B may be due to the increased migration of the larger Co^{2+} ions to the octahedral B-site instead of Fe^{3+} ions.

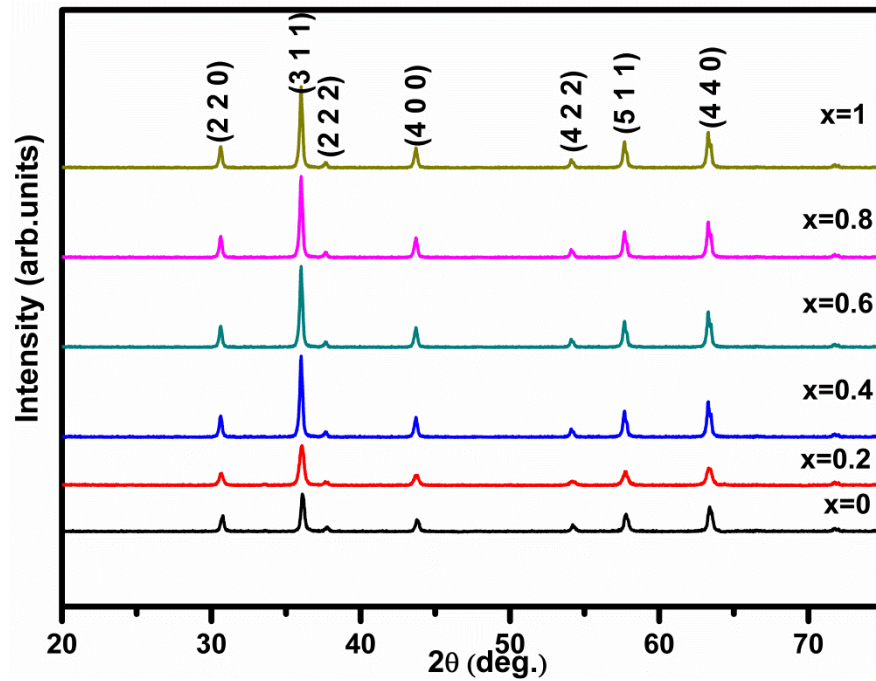


Fig. 1. XRD pattern of the $Co_{1-x}Zn_xFe_2O_4$ ($0 \leq x \leq 1$) nanoparticles synthesized at temperature $160^\circ C$ for 15 min.

Table 1. Variation of particle size and lattice constant (a) of $Co_{1-x}Zn_xFe_2O_4$ ($0 \leq x \leq 1$)

Composition 'x'	Particle size (nm) TEM	Particle size (nm) XRD	a (Å)
0	15.2	12	8.388
0.2	14.5	15	8.39
0.4	13.8	18	8.41
0.6	19.4	20	8.42
0.8			8.43
1			8.44

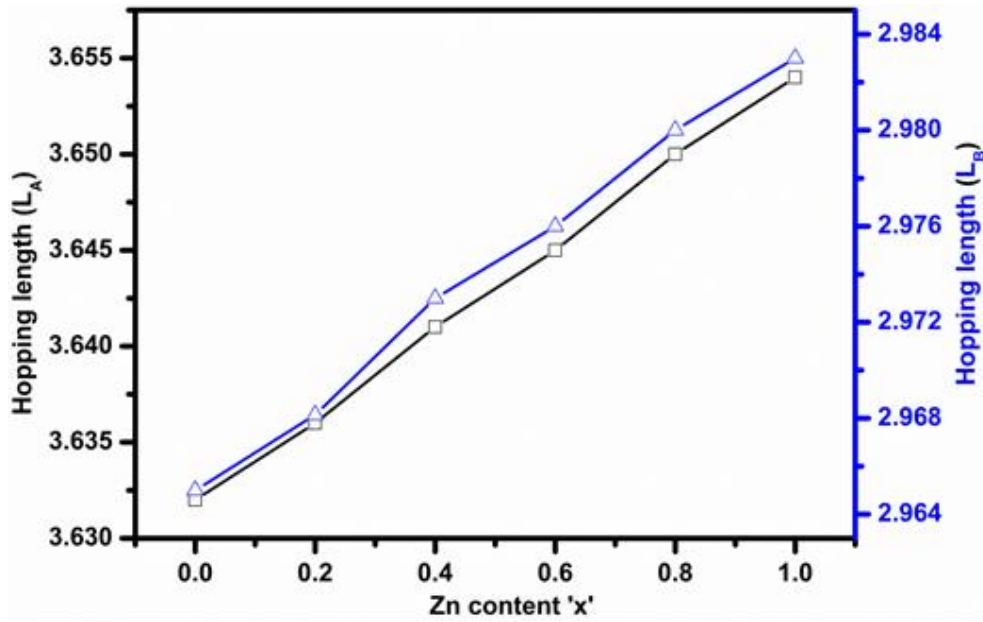


Fig. 2. Variation of hopping length (L_A and L_B) with composition for the system $\text{Co}_{1-x}\text{Zn}_x\text{Fe}_2\text{O}_4$.

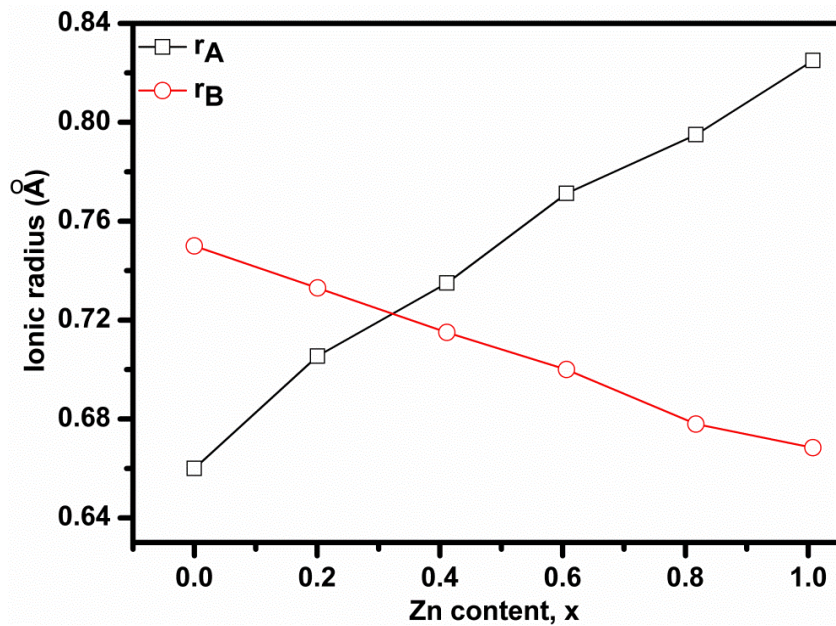


Fig. 3. Variation of ionic radius of the A-site (r_A) and of the B-site (r_B) of $\text{Co}_{1-x}\text{Zn}_x\text{Fe}_2\text{O}_4$.

3.2. Transmission electron microscope (TEM) analysis: The Selected Area Electron Diffraction (SAED) ring pattern (Fig. 4a) of the nanoparticles of $\text{Co}_{0.4}\text{Zn}_{0.6}\text{Fe}_2\text{O}_4$ is well resolved at (220), (311), (400), (422), (511), (440) reflections, as in XRD pattern. The samples exhibited more or less spherical morphology with uniform size. The lattice spacing of 0.24 nm corresponding to the (311) plane confirms the presence of crystalline $\text{Co}_{0.4}\text{Zn}_{0.6}\text{Fe}_2\text{O}_4$ particles (Fig. 4b). From Fig. 4c, TEM images of the particles are well separated from each other. The particle sizes of these samples are compared with those calculated from XRD and are listed in Table 1.

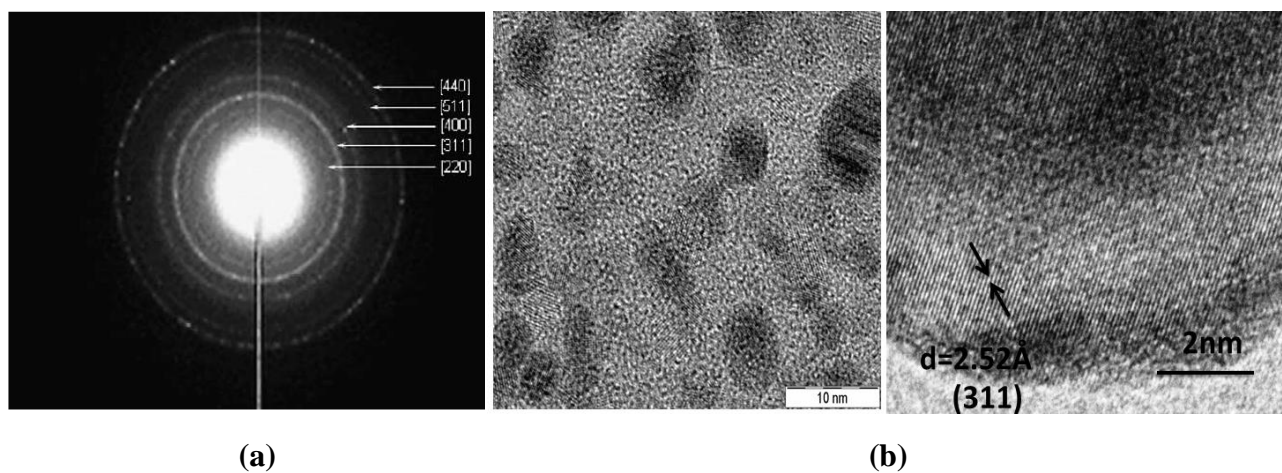


Fig. 4 (a). SAED pattern of $\text{Co}_{0.4}\text{Zn}_{0.6}\text{Fe}_2\text{O}_4$. **(b)** High magnification HRTEM image of $\text{Co}_{0.4}\text{Zn}_{0.6}\text{Fe}_2\text{O}_4$ showing the (311) oriented lattice planes.

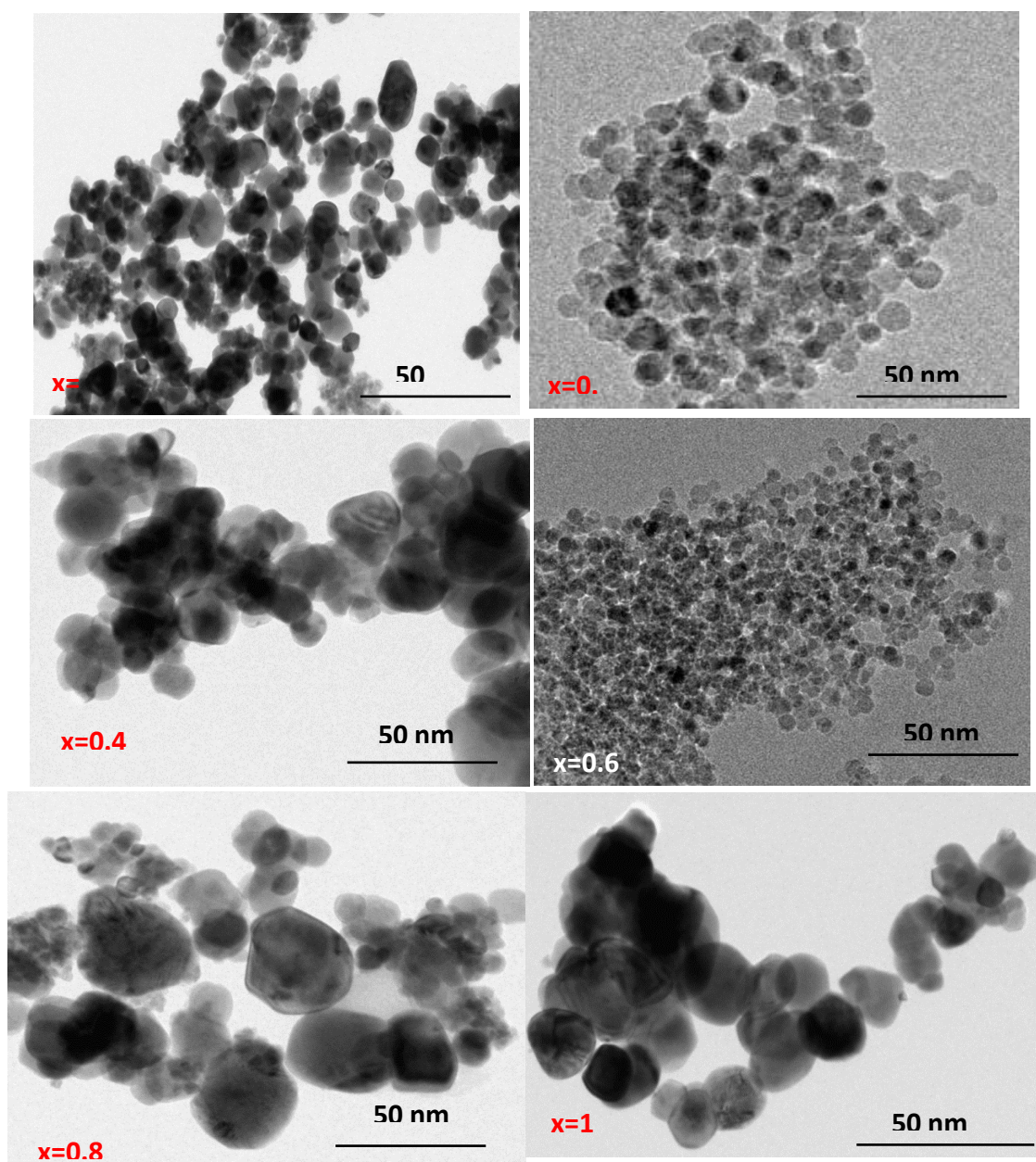


Fig. 4 (c). TEM images of $\text{Co}_{1-x}\text{Zn}_x\text{Fe}_2\text{O}_4$ ($0 \leq x \leq 1$) nanoparticles.

3.3. Fourier transform infrared spectroscopy (FTIR): FTIR spectra of as-synthesized nanopowders are presented in Fig. 5. Two main broad metal-oxygen bands are seen in the FTIR spectra of all spinels, and ferrites in particular. The highest one, ν_1 , is generally observed in the range 600–500 cm^{-1} , and it corresponds to intrinsic stretching vibrations of the metal at the tetrahedral site (T_d), $M_{\text{tetra}} \leftrightarrow O$, whereas the ν_2 lowest band is usually observed in the range 430–385 cm^{-1} , is assigned to octahedral metal stretching (O_h), $M_{\text{octa}} \leftrightarrow O$ [62–64, 4, 1]. We observed the band at 600 cm^{-1} is assigned as ν_1 ($M_{\text{tetra}} \leftrightarrow O$), near 400 cm^{-1} , ν_2 (430–385 cm^{-1}) and below 400 cm^{-1} . The absorption bands observed at ~ 3450 and ~ 1630 cm^{-1} prove the presence of adsorbed water on the surface of the ferrite nanopowders. The small absorption band at around 1380 and 1720 cm^{-1} in the as-prepared material may be assigned to the unreacted metallic salts and carbonyl respectively. Consequently, the ν_1 band observed at 561 cm^{-1} for ZnFe_2O_4 can be assigned to tetrahedral Zn^{2+} stretching and the ν_2 band observed at 425 cm^{-1} , involves the Fe^{3+} vibration at the octahedral site. The broad band (3600–2500 cm^{-1}) centered at 3430 cm^{-1} can be assigned to hydrogen-bonded O–H stretching vibration arising from surface hydroxyl groups on nanoparticles and adsorbed water. It seems that the ν_1 band shifts slightly toward the lower wave numbers with increase in ‘x’ over the composition range and indicating weakening of the metal–oxygen bonds in the tetrahedral sites due to the transition between the extent of normal spinel and inverse structures [65].

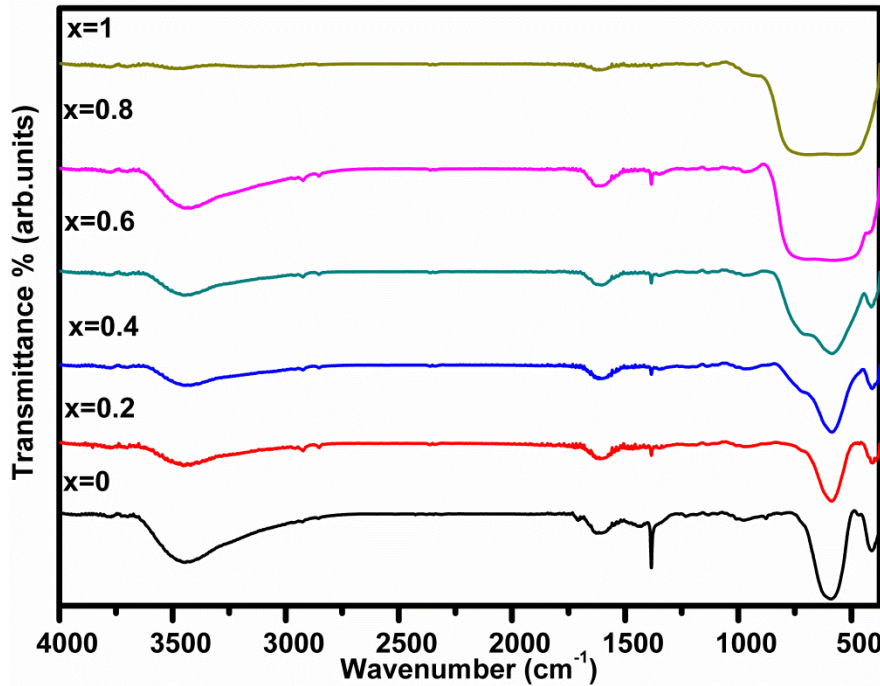


Fig. 5. FTIR spectra for as-prepared $\text{Co}_{1-x}\text{Zn}_x\text{Fe}_2\text{O}_4$ ($0 \leq x \leq 1$).

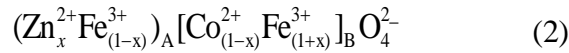
3.4. Room temperature M-H loops: Fig. 6 shows the variation of magnetization with the applied field. All prepared samples at room temperature exhibit ferrimagnetic coupling. As zinc is introduced in the system, it pushes Fe^{3+} ions from tetrahedral A sites to octahedral B sites [66]. This causes the increase in magnetization of $\text{Co}_{1-x}\text{Zn}_x\text{Fe}_2\text{O}_4$. That is, while the magnetic moment of the A site decreases due to increase of non-magnetic Zn ions in the A site, the magnetic moment of the B site increases due to increase of Fe^{3+} ions in B site. Therefore, in the present study, when the Zn concentration increases from 0 to 0.2, total magnetization ($M_{\text{oct}} - M_{\text{tet}}$) of $\text{Co}_{1-x}\text{Zn}_x\text{Fe}_2\text{O}_4$ increases due to the increase of inter-sublattice A–B super-exchange interaction between the magnetic ions of the sublattices A and B. This increase in saturation magnetization with Zn concentration from $x = 0.0$ to $x = 0.2$ is in good agreement with Neel’s collinear two-sublattice model [67]. Further, with increase in the Zn concentration from $x = 0.2$ to $x = 1.0$, the saturation magnetization gradually decreases from 79.04 emu/g to 26.04 emu/g. The results obtained are in well accordance with the

earlier reported values [68, 69]. The coercivity also decreases with Zn concentration which is attributed to the non-magnetic character of Zn ion. Since more Zn ions replace with Co ions by increasing 'x', the saturation magnetization and coercivity both decrease.

According to Neel's two sublattice model of ferromagnetism the magnetic moments of ions on the tetrahedral (A) and octahedral (B) sites are aligned antiparallel to each other and spins have collinear structure. Therefore, the theoretic magnetic moment per formula unit in μ_B , n_B^t , is described as

$$n_B^t(x) = M_B(x) - M_A(x) \quad (1)$$

where $M_B(x)$ and $M_A(x)$ are the B and A sublattice magnetic moments in μ_B , respectively. The cation distribution of the $\text{Co}_{1-x}\text{Zn}_x\text{Fe}_2\text{O}_4$ can be written as



As a function of Zn concentration, the theoretical magnetic moment values, n_B^t , of the $\text{Co}_{1-x}\text{Zn}_x\text{Fe}_2\text{O}_4$ were calculated using the cation distribution given in Eq. 2 and the ionic magnetic moments of Fe^{3+} , Co^{2+} , and Zn^{2+} as $4.85\mu_B$, $2.78\mu_B$ and $0\mu_B$, respectively. The experimental values of the magnetic moments (n_B^e), per unit formula in Bohr magneton (μ_B), were calculated according to the relation [70]:

$$n_B^e = \frac{M_w \cdot M_s}{5585} \quad (3)$$

where M_w is the molecular weight, M_s is the saturation magnetization and 5585 is the magnetic factor. The variation of the theoretic magnetic moment and experimental magnetic moment (n_B^t and n_B^e , respectively) with respect to Zn composition for $\text{Co}_{1-x}\text{Zn}_x\text{Fe}_2\text{O}_4$ is represented in Table 2. It is observed from the table that the theoretic magnetic moment increases linearly as a function of Zn concentration, and also the experimental magnetic moment, increases with Zn concentration of up to $x = 0.2$, and then gradually decreases with further increase in Zn concentration. This increase in n_B^e with Zn concentration of up to $x = 0.2$ can be attributed to the Neel's collinear two-sublattice model. However, this model is unable to explain the decrease of n_B^e (and hence M_s) with Zn concentration for $x > 0.2$. The decrease in n_B^t (and hence M_s) for $x > 0.2$ which results from the existence of non-collinear spin arrangement in the system could be explained on the basis of the three-sublattice model suggested by Yafet and Kittel [71].

When higher Co^{2+} ions are substituted by Zn^{2+} ions in the $\text{Co}_{1-x}\text{Zn}_x\text{Fe}_2\text{O}_4$, the magnetic ions of tetrahedral A site are so much decreased, the dominant inter-sublattice A–B super-exchange interaction becomes weaker and hence the intra-sublattice B–B super-exchange interaction strengthens, which in turn results in occurrence of random spin canting on the B site with respect to the direction of spins of the A site. Therefore, it is reasonable to conclude that the canted (non-collinear) spins lead to a decrease in the values of the experimental magnetic moment (and thus the magnetization) with Zn concentration for $x > 0.2$.

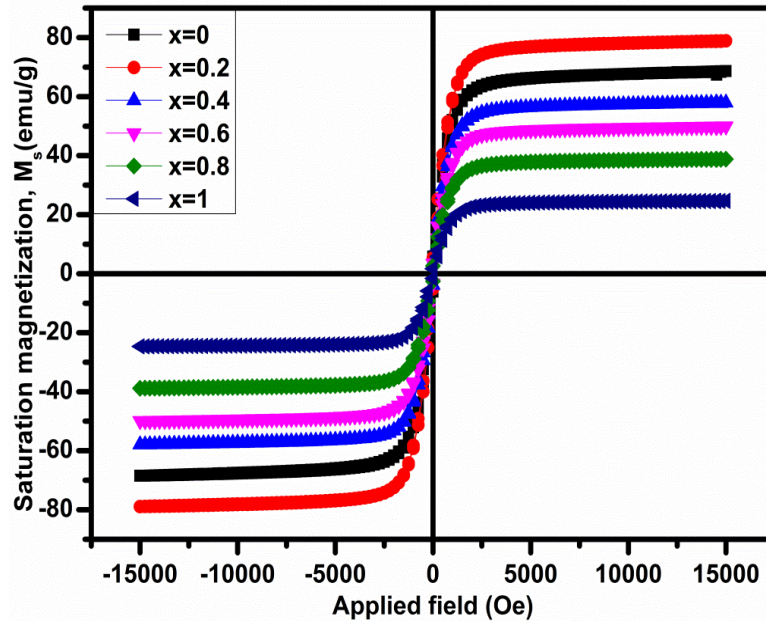


Fig. 6. The magnetic hysteresis loops of $\text{Co}_{1-x}\text{Zn}_x\text{Fe}_2\text{O}_4$ ($0 \leq x \leq 1$) at room temperature.

3.5. Y-K angles: The significant difference between the experimental and theoretical magnetic moment values which suggests that the magnetic order in the present ferrite system is not governed by the Neel-type magnetic order, but by the Y-K type magnetic order [72, 73]. According to the Y-K model, the B lattice can be divided into two sublattices B_1 and B_2 each having magnetic moments equal in magnitude and each oppositely canted at the same angle, α_{YK} , relative to the net magnetization at 0 K. In this way the two sublattices B_1 and B_2 have the triangular spin arrangement which becomes more significant with the changing concentration. The existence of canted spin and the behaviour of the magnetic moment with increasing Zn concentration can be observed by determining the Y-K angle (α_{YK}). The values of the Yafet and Kittle (Y-K) angle have been calculated using the formula:

$$n_B^e = M_B \cos \alpha_{Y-K} - M_A \quad (4)$$

Where n_B^e is the experimental magnetic moment expressed in the units of Bohr magneton and M_A and M_B are the Bohr magneton on the A site and B sites, respectively. The variation of the calculated Y-K angles for different concentrations of the system is shown in Fig. 7 and the values of the Y-K angles for each sample are listed in Table 2. The Y-K angle is zero for $x = 0.0$ indicating that the magnetization can be explained on the basis of the Neel's two-sublattice theory for only the sample with $x = 0.0$ in the present study. That is, CoFe_2O_4 shows a Neel-type of magnetic ordering. It is clear from Fig. 7 that the calculated values of the Y-K angles gradually increase with the increase of Zn concentration and finally extrapolate to 84.37° for the ZnFe_2O_4 ($x = 1.0$).

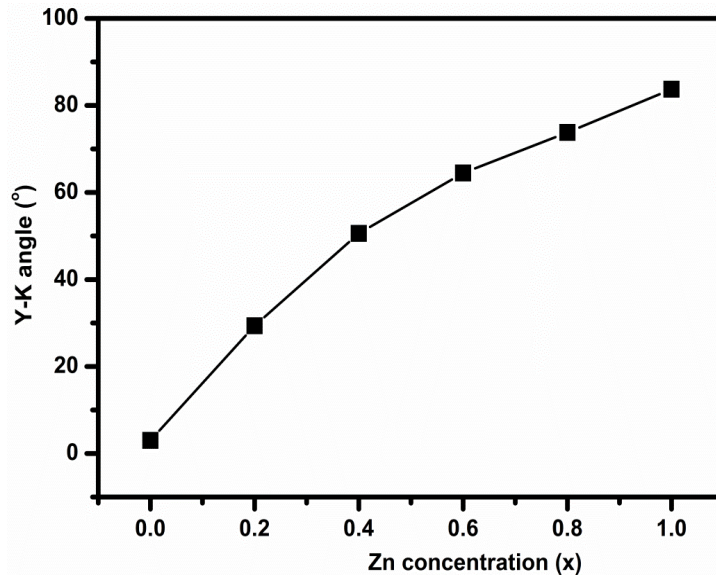


Fig. 7. The variation of Y-K angle with Zn concentration of $\text{Co}_{1-x}\text{Zn}_x\text{Fe}_2\text{O}_4$ ($0 \leq x \leq 1$).

Table 2. Data of saturation magnetization (M_s) for RT, magnetic moment (experimental and theoretical), Y–K angle (α_{YK}), blocking temperature (T_B) for $\text{Co}_{1-x}\text{Zn}_x\text{Fe}_2\text{O}_4$ system.

'x'	$M_s(\text{emu/g})$ RT	$\alpha_{Y-K}(^\circ)$	$n_B^e(\mu_B)$	$n_B^t(\mu_B)$	$T_B(\text{K})$
0	68.71	3.8	3.12	2.98	-
0.2	79.04	29.56	3.25	4.2	-
0.4	57.7	51.63	2.56	5.9	350
0.6	50.82	63.86	2.12	7.2	245
0.8	39.12	74.31	0.98	8.8	110
1	26.04	84.6	0.2	10.05	49.5

The non-zero Y-K angles suggest that for all the samples (for $x > 0$) the magnetization behaviour cannot be explained on the Neel two-sublattice model due to the presence of non-collinear spin structure on B sites, which strengthens the B–B interaction and thus decreases the A–B interaction. The increase in spin canting angles (Y–K angles) for the samples with $x > 0$ with increase in Zn content suggests the increased favour for triangular spin arrangements on B sites resulting in decrease of A–B exchange interaction and the existence of canted spin arrangements in all the samples (for $x > 0.0$) under consideration. Therefore, it leads to a reduction in saturation magnetization after Zn concentration with $x > 0.2$ and also increase of randomness and frustration show significant departure from the Neel-type collinear magnetic order. It is concluded from the evaluation of Y-K angles for $\text{Co}_{1-x}\text{Zn}_x\text{Fe}_2\text{O}_4$ ($0 \leq x \leq 1$) that the $\text{Co}_{1-x}\text{Zn}_x\text{Fe}_2\text{O}_4$ ($x > 0.0$) have a Y–K type magnetic order, while the CoFe_2O_4 NPs ($x = 0.0$) have a Neel-type magnetic order. In other words, in this study, all the Zn-doped cobalt ferrite nanoparticles show a Y–K type of magnetic ordering except the pure CoFe_2O_4 .

3.6. M-T analysis: Fig. 8 shows zero field cooled (ZFC) and field cooled (FC) curves of $\text{Co}_{1-x}\text{Zn}_x\text{Fe}_2\text{O}_4$ ($0 \leq x \leq 1$) measured in the temperature range of 10 - 400 K under an applied field of 50 Oe. Firstly, the samples were cooled down without any external magnetic field and then the magnetization of samples was recorded during heating up to 400 K under an applied field of 50 Oe. Later, the samples were cooled down again in an applied field of 50 Oe and then it was recorded during heating up to 400 K under an applied field of 50 Oe. As the temperature increases in ZFC measurement, firstly, the magnetic zero field cooling (MZFC) increases and then reaches a

maximum value at specific critical temperature, which is called the blocking temperature (T_B). Above T_B in the unblocked region, the MZFC monotonically decreases with increasing temperature. This is the characteristic behaviour of super-paramagnetic materials.

It is clear from Fig. 8, only the samples with Zn concentration of $0.6 \leq x \leq 1.0$ show super-paramagnetic behaviour at RT indicating that the magnetic interactions between the particles are weak and these samples can be regarded as good candidates for biomedical applications. The ZFC and FC measurements of all the samples except for the samples with Zn concentration ($x = 0.0$ and 0.2) show an irreversible magnetic behaviour below the temperature, called irreversibility (T_{irr}) temperature. T_{irr} is defined as the temperature at which the ZFC and FC curves split from each other and corresponds to the blocking temperature of the largest nanoparticles in the super-paramagnetic systems [74].

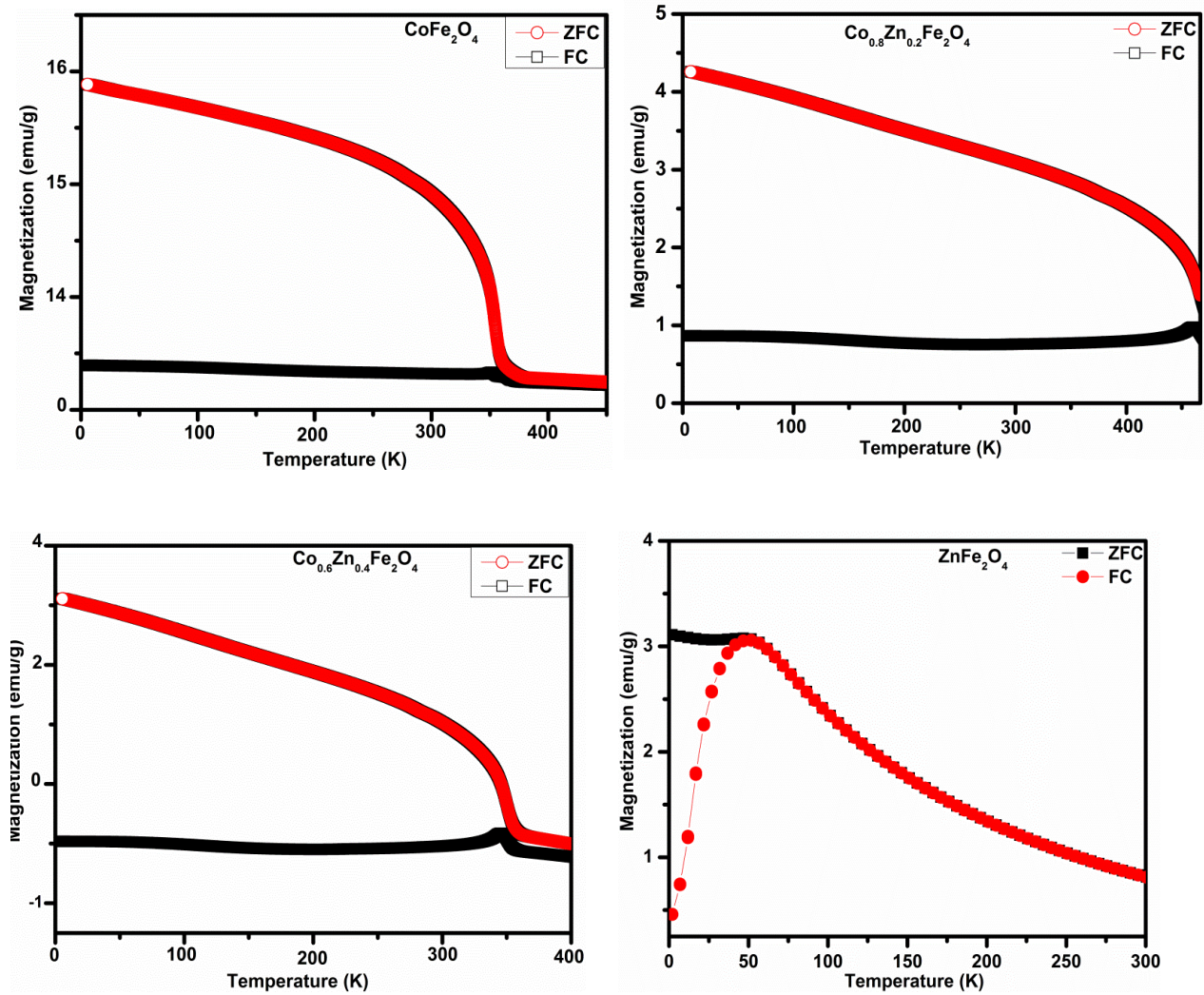


Fig. 8. Zero field cooled (ZFC) and field cooled (FC) curves of the $\text{Co}_{1-x}\text{Zn}_x\text{Fe}_2\text{O}_4$ under an applied magnetic field of 50 Oe.

Fig. 9 shows the variation of the coercive field (H_c) as a function of temperature. It could be easily seen that H_c strongly depends on both Zn concentration and temperature. Also H_c substantially increases with decreasing temperature. This is due to increase of effective magnetic anisotropy with decreasing temperature because the content of the Co^{2+} ions on the octahedral (B) sites increases with decreasing temperature [75]. In this study, the coercive field value of pure cobalt ferrite is 12585 Oe at 10 K, which is much larger than that of bulk CoFe_2O_4 (about 5 kOe at 5 K). At low

temperatures, the frozen surface spins resulting from coating material are strongly pinned with ordered core spins by exchange interactions and thus extra energy is needed to switch the ordered core spins. This interaction in the present system could be the reason for increase in coercive field at low temperatures [76]. Similar results have been reported in metal-substituted ferrite particles [77, 78].

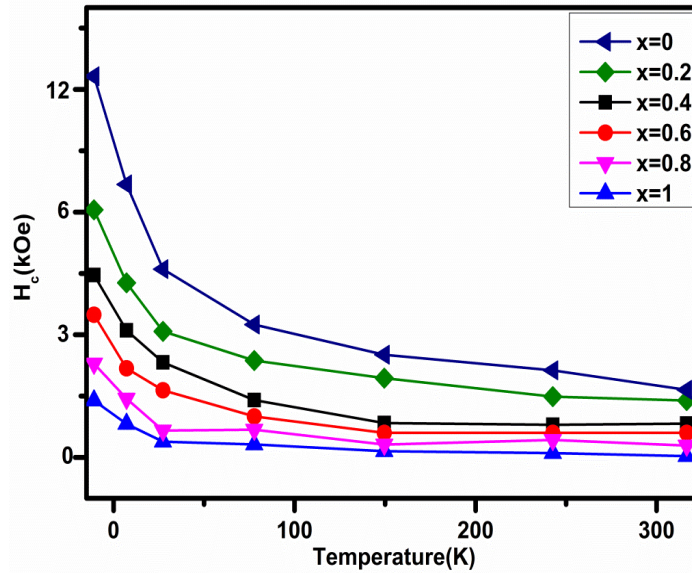


Fig. 9. Temperature dependence of the coercive field for $\text{Co}_{1-x}\text{Zn}_x\text{Fe}_2\text{O}_4$.

The variation of remnant magnetization (M_r) with Zn concentration at room temperature is depicted in Fig. 10. The inset shows the change in reduced remnant magnetization (M_r/M_s) with Zn concentration. The M_r/M_s gradually decreases with increasing Zn concentration and all M_r/M_s values are lower than the theoretical value of 0.5. As shown in the inset, for samples ($0.6 \leq x \leq 1.0$), M_r/M_s is approaching zero, which proves that these samples are super-paramagnetic at room temperature. This may be explained with decreasing magnetic anisotropy depending on the increasing Zn concentration [79]. According to the Stoner–Wohlfarth model [80], $M_r/M_s = 0.5$ for uniaxial anisotropy and $M_r/M_s = 0.832$ for cubic anisotropy.

These reduced remnant magnetization values plotted in the inset of Fig. 10 are more in agreement with uniaxial anisotropy rather than the expected cubic anisotropy according to the Stoner–Wohlfarth model. Therefore, all the samples used in this study have uniaxial anisotropy because of their reduced remnant magnetization values being lower than 0.5. Cobalt substituted ferrite nanoparticles with uniaxial anisotropy have been reported by some authors [81, 82]. The uniaxial anisotropy in magnetic nanoparticles can arise from surface effects [83]. The lower M_r/M_s values than 0.3 found for the samples with $x = 0.2$ and 0.4 in this study suggest that the interactions between the nanoparticles are not negligible [84].

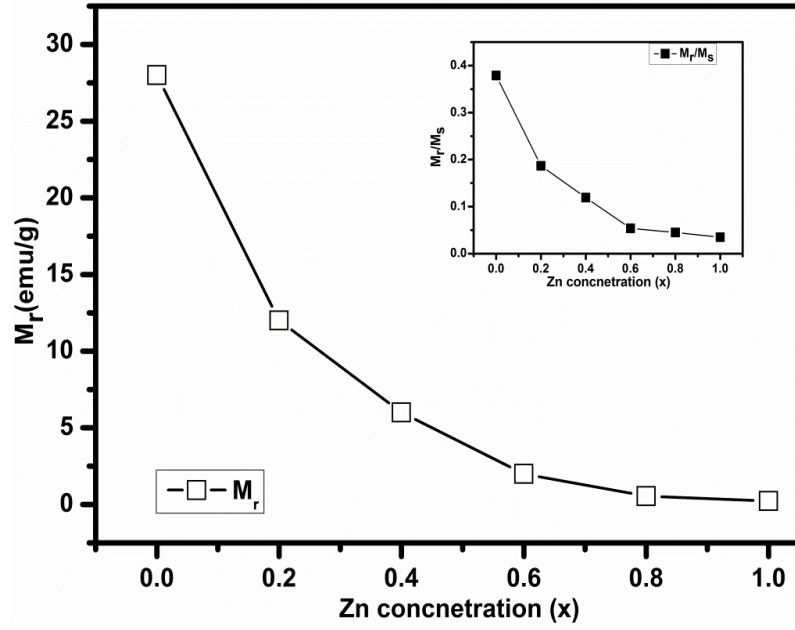


Fig. 10. The remnant magnetization versus Zn concentration taken at room temperature for the $\text{Co}_{1-x}\text{Zn}_x\text{Fe}_2\text{O}_4$ (inset presents the change in reduced remnant magnetization (M_r/M_s) with Zn content).

Fig. 11 shows the variation of the coercive field (H_c) and effective magnetic anisotropy constant (K_{eff}) with respect to Zn concentration at room temperature. It can be easily seen from figure that H_c and K_{eff} decrease with increasing Zn concentration. According to the Stoner-Wohlfarth model, H_c for an assembly of non-interacting 3D random particles is given by $H_c = 0.985 K_{\text{eff}}/M_s$ for uniaxial anisotropy and $H_c = 0.64 K_{\text{eff}}/M_s$ for cubic anisotropy. It was found from the M_r/M_s results that all the samples in this study have uniaxial anisotropy. Therefore, to calculate the K_{eff} , the relation $H_c = 0.64 K_{\text{eff}}/M_s$ was used. As shown in Figs. 9 and 11, H_c is almost negligible at room temperature for $0.6 \leq x \leq 1.0$, indicating the existence of super-paramagnetic behaviour for only these samples. The coercive field is associated to the strength of the magnetic field that is required to overcome the anisotropy barrier. According to the Stoner - Wohlfarth theory, magnetic anisotropy energy (E_A) for non-interacting single-domain particles is given by

$$E_A = KV \sin^2 \theta \quad (5)$$

where K , V , and θ are magnetic anisotropy energy constant, volume of the particles and the angle between magnetization direction and the easy axis of a nanoparticles, respectively. With reducing of magnetic anisotropy, the magnetic anisotropy energy barrier (E_A) decreases, which causes lower external magnetic field for spin reversal. The strong magneto-crystalline anisotropy of cobalt ferrite is mainly due to the presence of Co^{2+} ions in the octahedral (B) sites of the spinel structure [85]. When the Zn concentration increases in cobalt ferrite the concentration of the Co^{2+} ions in the octahedral (B) sites decreases, which leads to decrease in effective magnetic anisotropy. Therefore, in this study, the effective magnetic anisotropy, K_{eff} and accordingly H_c of the samples decrease with increasing Zn concentration. The decrease of K_{eff} and H_c with increasing Zn concentration is generally expected behaviour in metal-substituted ferrite particles [86, 77].

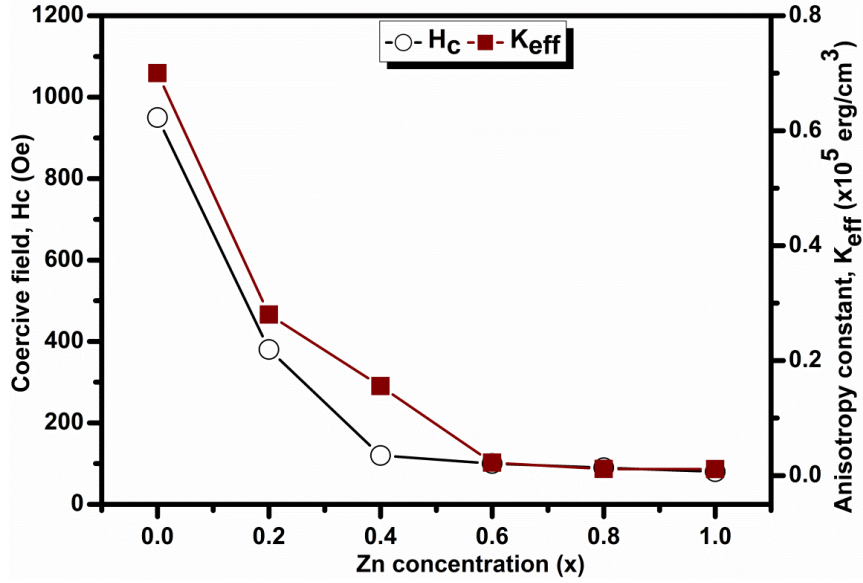


Fig. 11. Composition dependence of coercive field (H_c) and effective magnetic anisotropy constant (K_{eff}) of $Co_{1-x}Zn_xFe_2O_4$ at room temperature.

At blocking temperature (T_B), the magnetic anisotropy energy barrier of the single-domain nanoparticles, $K_{eff} V$ is overcome by thermal energy kT_B , where K_{eff} and V are magnetic anisotropy energy constant and volume of the particles, respectively, k is the Boltzmann constant and T_B is the blocking temperature and then the spins fluctuate randomly above T_B . The T_B values of the samples are listed in Table 2. It is observed from the ZFC and FC measurements in Fig. 8 that the T_B of only the $0 \leq x \leq 0.2$ is higher than 400 K because of higher effective magnetic anisotropy and T_B of $0.4 \leq x \leq 0.6$ gradually decreases with increasing Zn concentration. It is known that the blocking temperature depends on the effective magnetic anisotropy. As seen from Fig. 11, the anisotropy constant continuously decreases as a function of Zn concentration. Therefore, the blocking temperature decreases with increasing Zn concentration. It has been widely reported that the magnetic interactions such as dipole-dipole interactions between the particles and exchange interactions between surface spins and core spins of the nanoparticles play an important role in determining the magnetic properties of the particles [87, 88]. The stronger dipolar interactions also result in the increase in the blocking temperature. As well as a decreasing magnetic anisotropy, and a weakening of dipolar interactions at high Zn concentrations is another reason for the reducing blocking temperature.

2. Synthesis of $Ni_{0.4}Zn_{0.2}Mn_{0.4}Fe_2O_4$

The energy to form the Ni-Zn-Mn ferrite nanocrystallites is provided by oxidation-reduction process of thermal precursor and fuel in the sol-gel auto-combustion process [89]. Metal nitrates were employed in this process as they have a dual role of being a soluble cation source and the oxidant [90]. Citric acid was used with 2 important roles: the fuel for the combustion reaction and as a chelating agent to form complexes with metal ions, preventing the precipitation of hydroxylated compounds [91].

The materials used were nickel nitrate hexahydrate (99.99 %, Aldrich), zinc nitrate hexahydrate (98%, Aldrich), manganese nitrate hexahydrate (99.5%, Aldrich), iron nitrate monohydrate (98%, Aldrich) and citric acid monohydrate (99%, Merck, India). The synthesis was achieved by mixing stoichiometric proportions of the respective nitrates and citric acid. For each nitrate, was taken a solution called citrate precursor. First citric acid was dissolved in distilled water in the ratio 1:3 (mol %) relative to the corresponding metal nitrate under magnetic stirring and heating to 60°C.

The next step was to add mass nitrate still under magnetic stirring and heating until complete formation of the metal complex reaction with citric acid, forming metallic citrate resulting in a clear and stable solution. With constant stirring the pH of the solution was adjusted to about 7 with ammonia. The resulting mass was subjected to auto-combustion on a hot plate at 200°C for 2h, there by releasing the large amount of gases (CO₂, H₂O, N₂), and auto-combustion occurred giving rise to a dark brown ferrite powder. And the powder was subsequently ground for further heat treatment and structural characterizations.

The TG/DTG curve was obtained in a thermo-balance Perkin Elmer Model TGA 7 HT in a nitrogen atmosphere at a heating rate of 5°C/min in the temperature range 25-1100°C. To confirm the phase formation for the as-prepared samples, a Phillips PANalytical X'pert powder X-ray diffractometer (XRD) was used, with Cu K_α (radiation wavelength $\lambda = 1.54\text{\AA}$). Parameters such as crystallite size, the lattice parameters and the position of the ions in the structure were obtained using the Rietveld method. The particle size and morphology of the powders were studied using the transmission electron microscope (Model JEM-2010, JEOL, Tokyo, Japan). The ferrite powders were pressed into pellets and toroidal specimens using a 1500 Kg/cm² pressure by adding polyvinyl alcohol (PVA) 2 wt% as binder. Here we have made an attempt of optimising the sintering temperature of this particular composition Ni_{0.4}Zn_{0.2}Mn_{0.4}Fe₂O₄, sintering at 400, 500, 600 and 700°C for 4h using conventional sintering method. Magnetic measurements were made using a vibrating sample magnetometer (VSM), Lakeshore 7500, USA. The incremental permeability and Q-factor under dc-bias-superposition conditions were measured by means of a precision LCR meter (Agilent 4284A) with a dc bias current source (N9936A).

3. Results and Discussions of Ni_{0.4}Zn_{0.2}Mn_{0.4}Fe₂O₄ Ferrite

5.1. Thermo-gravimetric analysis: Fig. 12 shows the thermo-gravimetric analysis of Ni_{0.4}Zn_{0.2}Mn_{0.4} ferrite. The TGA-DTG curves indicate that the degradation of dried gel show multi-step weight loss. The first stage of degradation can be observed between 26 and 200°C, with respect to the output of waste water which is adsorbed on the material during the synthesis step, the step of degradation can be best viewed through the DTG curve, which should be the derivative of the TGA, broadens the mass losses that are subtly displayed in the TGA curve.

The second stage of degradation occurs between 200-550°C, which is related to structural water and traces of NO, NO₂, CO and CO₂. The third stage of degradation occurs between 550 and 1000°C, this loss is related to the output of volatile organics still remaining in the material after 1000°C. A continuous line in the TGA curve is related to the end of the degradation of organic matter and the formation of oxides can be observed indicating formation of 100% crystalline phase and ceramic yield of about 90%.

In aqueous chemistry, the degree of condensation varies with different ligand types and the formation of ligands in turn depends on the pH region [92]. As the pH value of the aqueous solution was modified to 7, better condensation process during hydrolysis provided single step decomposition to form the nanocrystallites. The weight loss for precursor occurs in two steps. In fact, O-H groups, carboxyl group and NO₃⁻ ions exist in the dried gel [93]. The first weight loss represents the water vaporization of O-H groups. In the second step, a large weight loss represents the decomposition of carboxyl, NO₃⁻ ions and NH₄NO₃, and at the same time, auto-combustion occurred. The decomposition of NH₄NO₃ supplied oxygen to accelerate the combustion reaction [94]. As the decomposition of NH₄NO₃ is endothermic process, the combustion temperature is decreased and the amount of heat generated in the combustion process is also decreased. Therefore, the decomposition of NH₄NO₃ favours the formation of small size crystallites in this synthesis.

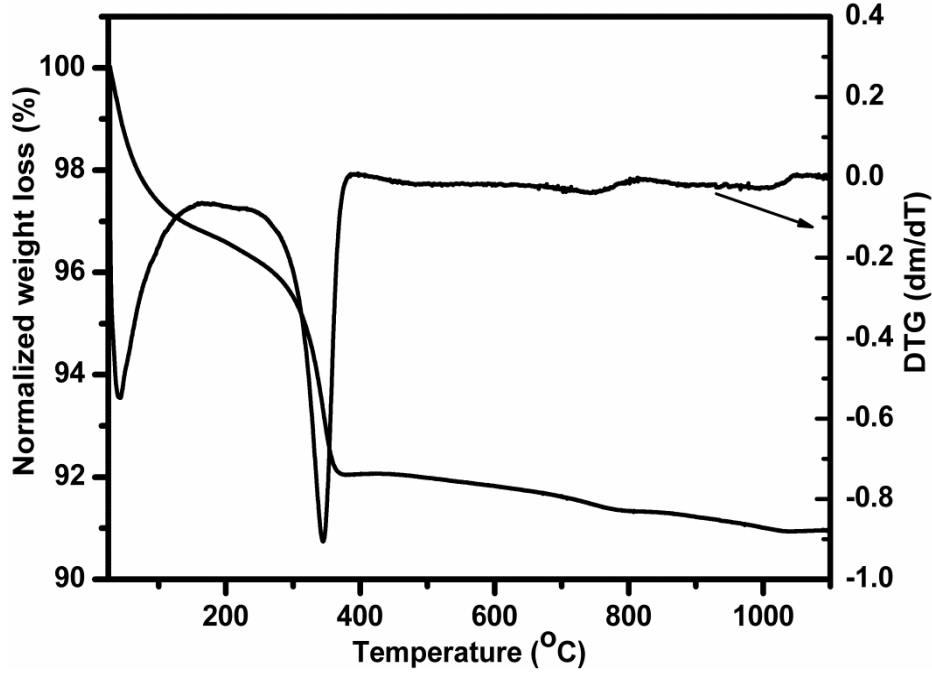


Fig. 12. TGA-DTG of $\text{Ni}_{0.4}\text{Zn}_{0.2}\text{Mn}_{0.4}\text{Fe}_2\text{O}_4$ of dried gel.

5.2. X-ray diffraction and Rietveld refinement: Fig.13 shows the X-ray diffraction of ferrite $\text{Ni}_{0.4}\text{Zn}_{0.2}\text{Mn}_{0.4}\text{Fe}_2\text{O}_4$ sintered at 300°C, 400 °C, 500°C, 600°C and 700°C for 4h. The peaks indicate the formation of single phase spinel. The formation of single phase spinel type was achieved by controlling the atmosphere using argon. By analyzing only the ferrite phase, an increase in peak intensity with increasing calcination temperature can be noted. This is due to the fact that diffusion occurs more readily at higher temperatures, resulting in better organization of the system, which increases the amount of crystalline phase formation observed in the diffraction peaks with better definition and more intensity. The data obtained from X-ray analysis were quantified using the Rietveld mathematical treatment. By this method, it was possible to quantify the phases formed, and to determine the crystallite size.

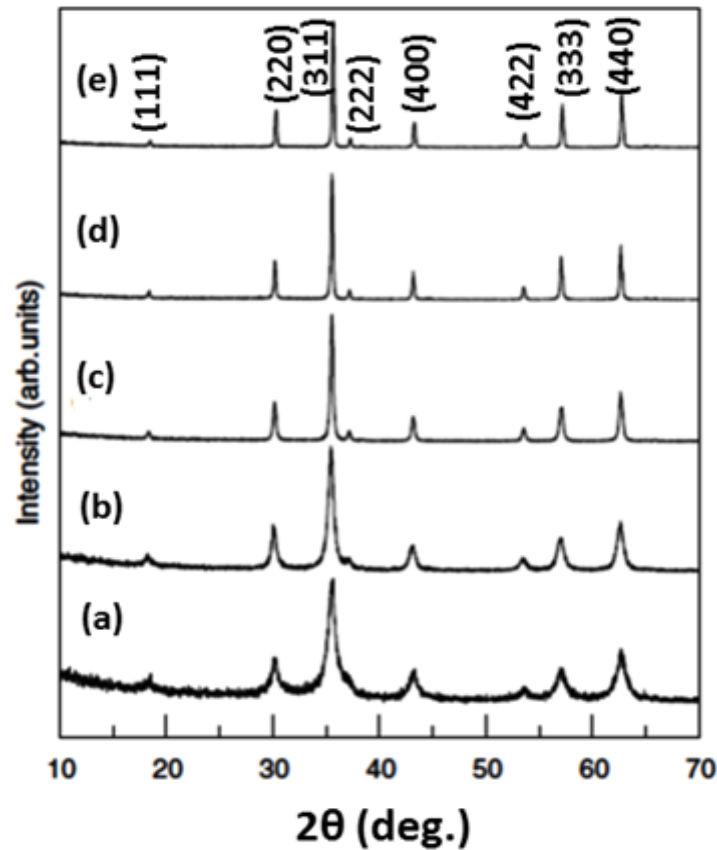
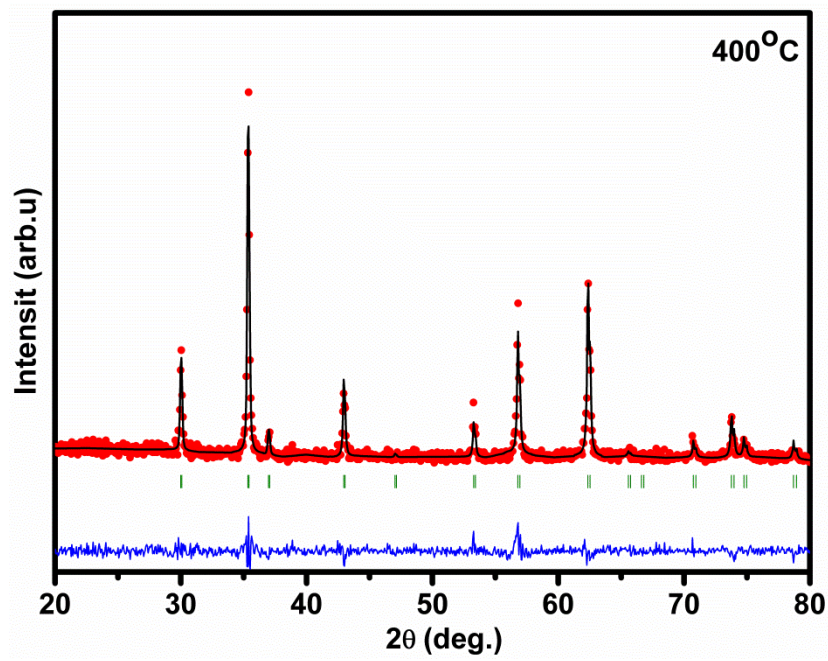


Fig. 13. XRD patterns of $\text{Ni}_{0.4}\text{Zn}_{0.2}\text{Mn}_{0.4}\text{Fe}_2\text{O}_4$ powder sintered at (a) 300 °C, (b) 400 °C, (c) 500 °C, (d) 600 °C, and (e) 700 °C.

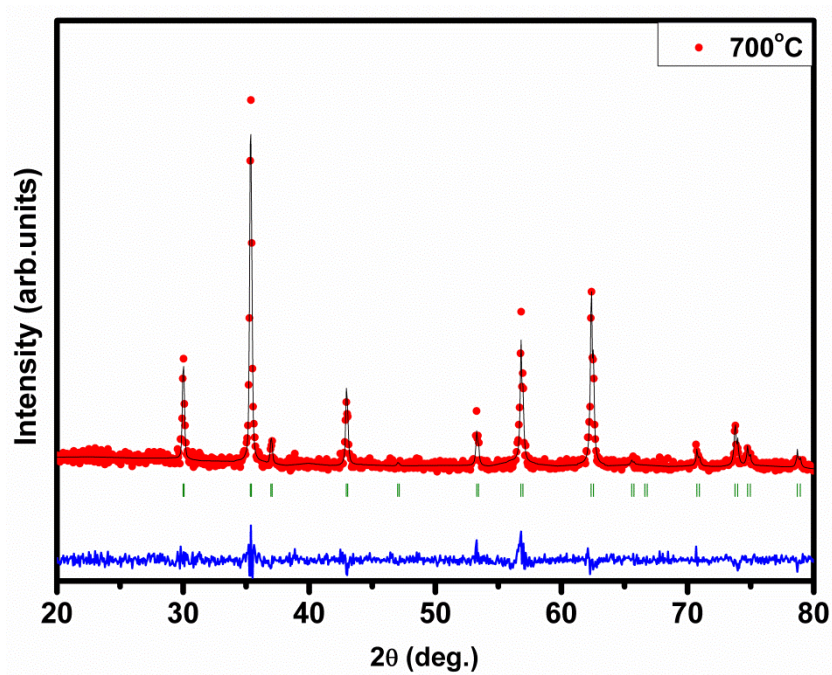
The calculated diagram (Fig. 14) is based on crystallographic structure models, which also take into account specific instrument and sample effects. The parameters of this model have been refined simultaneously using least-squares method in order to obtain the best fit to all measured data. By least squares refinement, a so-called figure-of-merit function R has been defined, which describes the residual (agreement) between observed and calculated data. It is noteworthy that many different statistical R factors have been proposed for judging the quality of a Rietveld refinement.

The R factors show the mean deviation from the model in per cent. The “profile R-factor”, R_p , and “weighted profile R-factor”, R_{wp} , for all the refinements are presented in Table 3. The values of R_{wp} as obtained in the present investigation are well within the limits of experimental accuracy. Fig. 14 shows the standard X-ray diffraction measured (red circles) and calculated (black line) by Rietveld for $\text{Ni}_{0.4}\text{Zn}_{0.2}\text{Mn}_{0.4}\text{Fe}_2\text{O}_4$ ferrite sintered at (a) 400°C and (b) 700°C for 4h, respectively.

It could be seen from the Table 4 that as the sintering increases there is increase in the average crystallite size (D) from 18 nm to 30 nm. Increasing the sintering temperature causes a greater diffusion between grains, increasing the average size of the crystals. The value of lattice constant increases from 8.271 Å to 8.298 Å with an increase of sintering temperature and the lattice parameters are matching well with the values obtained from refinement. Data of lattice constant calculated using the characteristic peak (311) matches with that obtained using Rietveld refinement.



(a)



(b)

Fig. 14. Standard X-ray diffraction measured (red circles) and calculated (black line) by Rietveld for Ni-Zn-Mn ferrite sintered at: (a) 400°C for 3h, and (b) 700°C for 2h.

Table 3. Results of Rietveld refinement of $\text{Ni}_{0.4}\text{Zn}_{0.2}\text{Mn}_{0.4}\text{Fe}_2\text{O}_4$ powder sintered at different temperatures.

Temperature	χ^2	R_{wp}	R_p
400°C	1.12	0.013	0.010
500°C	1.24	0.027	0.018
600°C	1.70	0.029	0.019
700°C	1.95	0.039	0.022

Table 4. Values of lattice constant, strain, bulk and x-ray densities, porosity, and crystallite size.

Temperature	Lattice Constant (Å)	Lattice constant (Å) from refinement	Strain (%) from refinement	Bulk density(d_b) (g/cc)	X-ray density(d_x) (g/cc)	Porosity (%)	Particle size (nm) TEM
As-prepared	8.271	8.26	1	4.61	5.02	9	18
400°C	8.283	8.27	0.2	5.02	5.22	4	22
500°C	8.286	8.28	0.1	5.15	5.30	3	24
600°C	8.293	8.29	0	5.36	5.45	2	26
700°C	8.298	8.30	0	5.60	5.50	2	30

5.3. Transmission Electron Microscopy: Fig. 15(a-d) shows the TEM images of $\text{Ni}_{0.4}\text{Zn}_{0.2}\text{Mn}_{0.4}\text{Fe}_2\text{O}_4$ sintered at different temperatures, which demonstrates that these samples are in nano-regime. TEM images show better crystallinity as well as regular shape (spherical) and size of particles. However, the crystalline powders are easy to form agglomerates due to nanosize effect and intrinsic magnetism. In order to disperse particles, samples are grinded. The grain size estimated from TEM pictures is slightly lower than the calculated crystallite size. The average particle size from TEM studies was found to be around 18-30 nm. The lattice spacing of 0.32 nm corresponding to the (311) plane is shown in Fig. 15(e). The d-values computed from the XRD and the SAED pattern (Fig. 15(f)) matches well with the standard d-values of Ni-Zn ferrite [95] (JCPDS #00-052-0278).

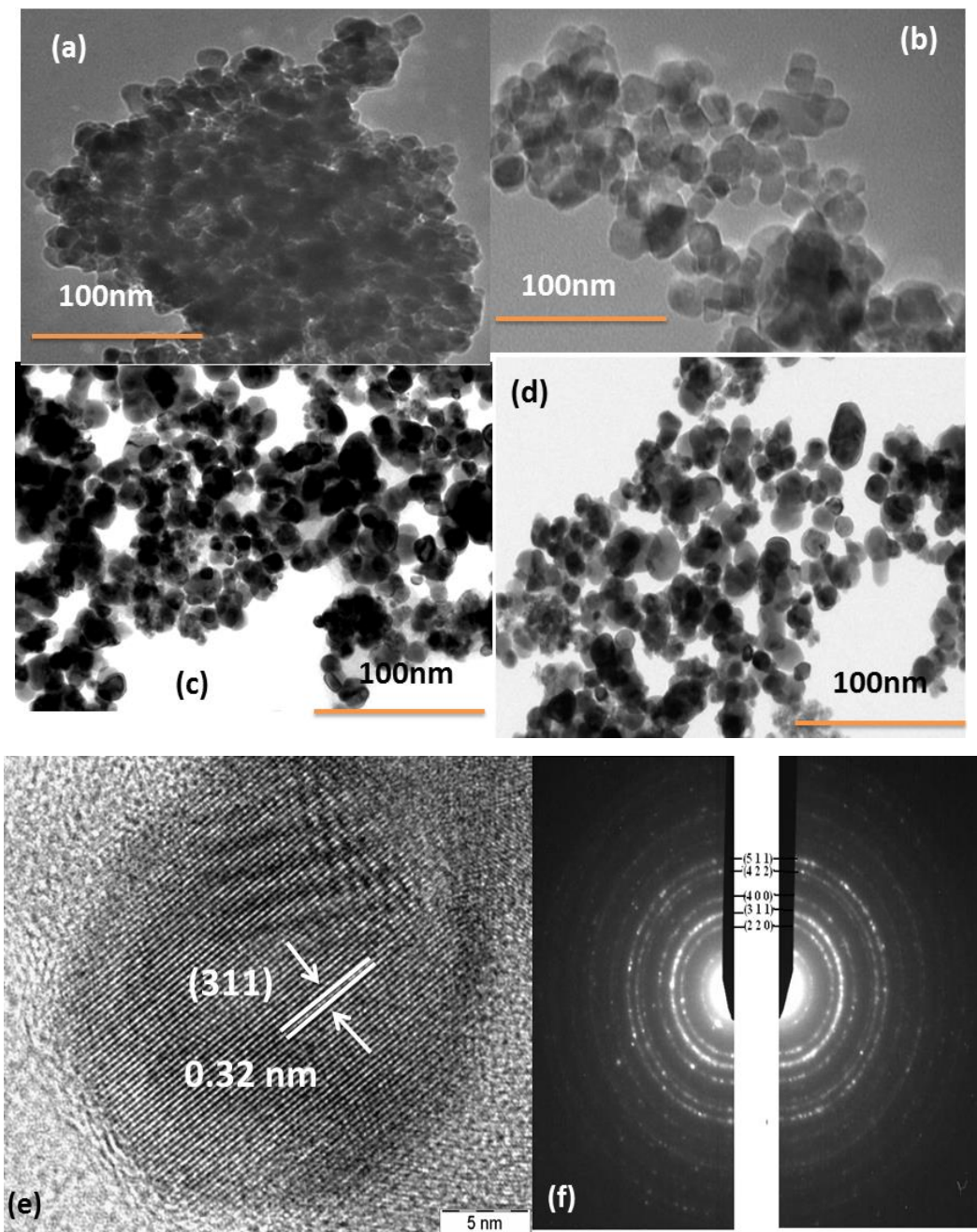


Fig. 15. TEM images of $\text{Ni}_{0.4}\text{Zn}_{0.2}\text{Mn}_{0.4}\text{Fe}_2\text{O}_4$: (a) as-prepared powder, (b) sintered at 500°C, (c) 600°C, (d) 700°C, (e) High magnification HRTEM image of 700°C showing the (311) oriented lattice planes of $\text{Ni}_{0.4}\text{Zn}_{0.2}\text{Mn}_{0.4}\text{Fe}_2\text{O}_4$, and (f) SAED pattern of d-spacing matched with XRD.

5.4. Room temperature M-H loops: Fig. 16 shows the dependence of the magnetization as a function of applied magnetic field through the hysteresis loops for $\text{Ni}_{0.4}\text{Zn}_{0.2}\text{Mn}_{0.4}\text{Fe}_2\text{O}_4$ sintered at different temperatures. The loops are exhibiting low power loss and low coercivity. The low losses in the reversal magnetic field indicate that it is a soft magnetic material being disengaged little energy to reverse the magnetic moment. The magnetic parameters such as saturation magnetization, remnant magnetization, and coercive field, calculated from the hysteresis curve are arranged in the Table 5. The saturation magnetization values increased with increasing sintering temperature, ranging from 23.91 to 55.80 Am^2/Kg , to the powders sintered at 400 to 700°C for 4h, respectively. The same happened with the coercive field, changing from 4.79 to 6.39 kA/m for the sintered powder samples. The squareness factor (M_r/M_s) also monotonically increases with sintering

temperature (Table 5), suggesting an increase in magneto-crystalline anisotropy. We believe this increase in magneto-crystalline anisotropy is most likely due to improvement in crystal order and structure, expected in samples sintered at high temperatures.

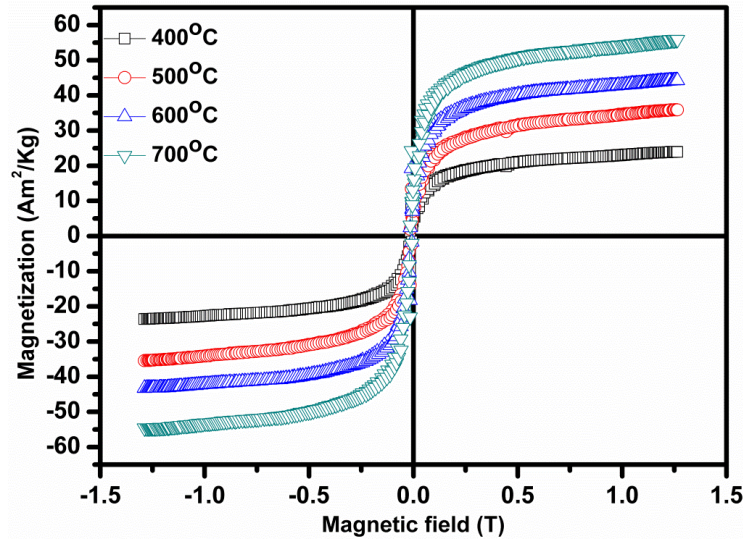


Fig. 16. Magnetic Hysteresis loops of $\text{Ni}_{0.4}\text{Zn}_{0.2}\text{Mn}_{0.4}\text{Fe}_2\text{O}_4$

Table 5. Remnant magnetization (M_r), saturation magnetization (M_s) and coercive field (H_c) of $\text{Ni}_{0.4}\text{Zn}_{0.2}\text{Mn}_{0.4}\text{Fe}_2\text{O}_4$ sintered at different temperatures. As temperature increases M_r , M_s and H_c increase.

Temperature	M_s (Am^2/Kg)	M_r (Am^2/Kg)	H_c (kA/m)	$\Delta M(M_s - M_r)$ (Am^2/Kg)	M_r/M_s
400°C	23.91	9.10	4.79	14.81	0.38
500°C	35.87	13.43	5.58	22.44	0.37
600°C	44.26	19.01	5.90	25.25	0.42
700°C	55.80	24.44	6.39	31.36	0.43

5.5. Magnetic field dependent permeability: Fig. 17 shows the variation of incremental permeability (tested at 100 kHz) with superposition magnetic field. Permeability first increased for all the samples as the sintering temperature increased, without dc-bias-superposition, which was mainly due to the increase of sintered density and average grain size. With increasing dc-bias-superposition magnetic field, the permeability of all samples decreased continuously.

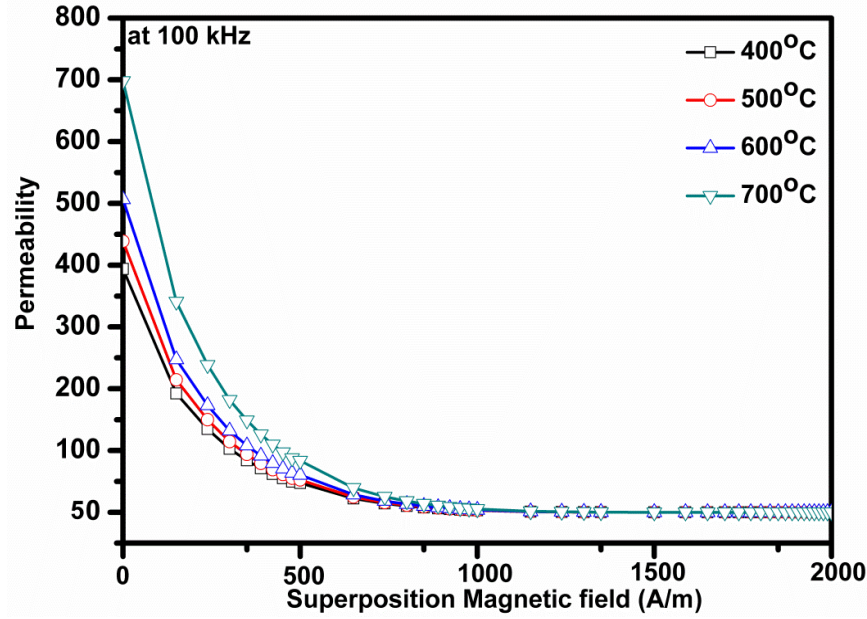


Fig. 17. Variation of permeability with superposition magnetic field.

5.6. Magnetic field dependent quality factor: Fig. 18 shows the variation of Q-factor (tested at 100 kHz) with superposition magnetic field for the four samples. The Q-factor first increased with the superposition magnetic field, attaining a maximum at 600 A/m, and then it continuously decreased upon further increasing the superposition magnetic field for all samples. Hence, it could be concluded that a sample that was well sintered and had an even and relatively small average grain size was favourable for attaining better performance in terms of dc-bias-superposition characteristics [96].

To demarcate the intrinsic relationship between microstructure and dc-bias-superposition characteristics, M_r , M_s , H_c and density of the samples were measured. The sample sintered at 400°C has low values of M_s and M_r owing to the fact that it was not well sintered. As the sintering temperature increases, all the parameters M_r , M_s and H_c increase as well as the density also rises, minimizing the porosity of the samples.

It is known that higher M_s and ΔM favour a higher incremental permeability [97]. As the temperature increases, permeability increased and the behaviour is explained above. The Q-factor is determined by density and microstructure. Higher density favours a higher Q-factor. The microstructure with an even and single domain grain size also favours a higher Q-factor. According to Snoek's law, permeability is inversely proportional to the cut-off frequency of ferrites. And the frequency at which the Q-factor attained the maximum value is proportional to the cut-off frequency of ferrites.

In this study, the Q-factor was tested at 100 kHz, although this was not the frequency at which the peak Q-factor appeared. The samples could attain higher Q-factor values at less than 100 kHz. With the increase of superposition magnetic field, incremental permeability decreases; the cut-off frequency and the frequency at which the peak Q-factor appeared gradually shifted to higher values. Hence, with appropriate superposed magnetic field, the frequency at which the peak Q-factor appeared just shifted to 100 kHz, so the Q-factor increased. Thereafter, the frequency at which the peak Q-factor appeared shifted to higher values, so the Q-factor at 100 kHz also gradually decreased.

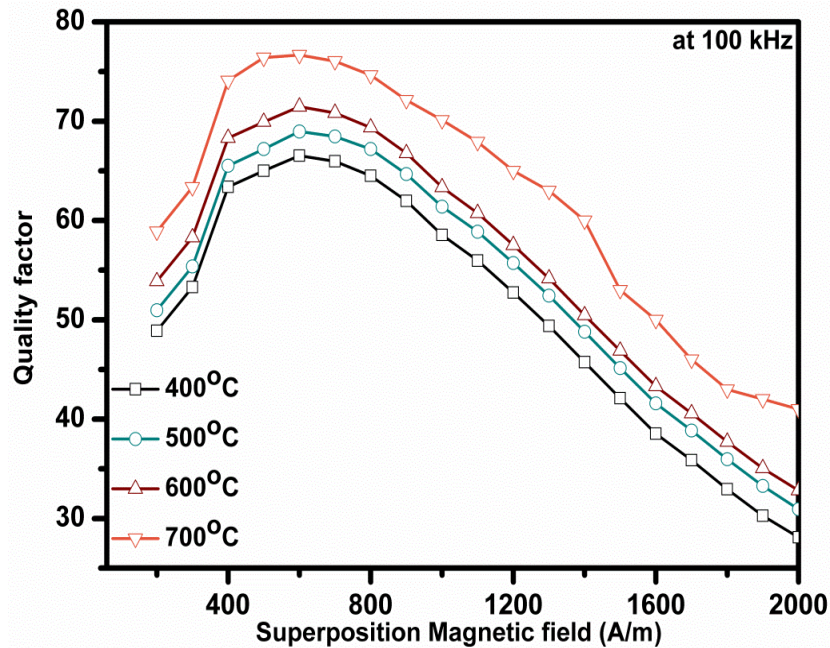


Fig. 18. Variations of Q-factor with superposition magnetic field.

6. Conclusions

The presence of Zinc ions causes appreciable changes in the structural and magnetic properties of Zn-substituted CoFe_2O_4 synthesized by microwave hydrothermal route. All the nanocrystals exhibit cubic spinel structure. This extensive study of magnetic properties of Co-Zn ferrites confirms that these materials are suitable and good candidates for hyperthermia applications. Zero field cooled (ZFC) and Field cooled (FC) measurements reveal that samples with $0.6 \leq x \leq 1$ have superparamagnetic behaviour at room temperature, which shows weak interaction between magnetic particles. The blocking temperature obtained from ZFC-FC curves decreases as Zn concentration increases. Lower reduced remnant magnetization (M_r/M_s) values ($x < 0.5$) suggest that all the samples have uniaxial anisotropy. It was found that the effective magnetic anisotropy, the coercivity and remnant magnetization continuously decrease with increasing Zn concentration. The blocking temperature decreases with Zn concentration.

The results specify that the auto-combustion method was effective in getting the single phase of $\text{Ni}_{0.4}\text{Zn}_{0.2}\text{Mn}_{0.4}\text{Fe}_2\text{O}_4$. The average crystallite size increased linearly with the calcination temperature. Increasing the crystallite size is related to increased diffusion effect caused by the increase of the sintering temperature. The hysteresis loops showed soft magnetic behaviour. Consequently, the sample that was well sintered and had a microstructure that consisted of relatively small and even grains favoured the attainment of better dc-bias-superposition characteristics, including permeability and Q-factor. With the addition of Mn to Ni-Zn ferrites, there is not much change in its structure, but it increases its permeability and it is stable up to 600 kA/m of dc-bias superposition magnetic field; so these materials can be used in high frequency power applications as they have very high resonant frequency.

References

- [1] J. Smit, H.P.J. Wijn. Ferrites, Philips Technical Library, Eindhoven, 1959.
- [2] V.G. Harris, A. Geiler, Y. Chen, et al. Recent advances in processing and applications of microwave ferrites, *Journal of Magnetism and Magnetic Materials* 321(14) (2009) 2035–2047.

- [3] Y. Qu, H. Yang, N. Yang, et al. The effect of reaction temperature on the particle size, structure and magnetic properties of co-precipitated CoFe_2O_4 nanoparticles, *Materials Letters* 60(29–30) (2006) 3548–3552.
- [4] N. Kasapoglu, B. Birsoz, A. Baykal, Y. Koseoglu, M.S. Toprak, Synthesis and magnetic properties of octahedral ferrite $\text{Ni}_x\text{Co}_{1-x}\text{Fe}_2\text{O}_4$ nanocrystals. *Central European Journal of Chemistry* 5(2) (2007) 570–580.
- [5] S.W. Cao, Y.J. Zhu, G.F. Cheng, et al, ZnFe_2O_4 nanoparticles: microwave-hydrothermal ionic liquid synthesis and photocatalytic property over phenol, *Journal of Hazardous Materials* 171 (1–3) (2009) 431–435.
- [6] Y.L. Liu, Z.M. Liu, Y. Yang, et.al, Simple synthesis of MgFe_2O_4 nanoparticles as gas sensing materials. *Sensors and Actuators B: Chemical* 107(2) (2005) 600–604.
- [7] H. Igarash, K. Okazaki, Effects of porosity and grain size on the magnetic properties of NiZn ferrites, *J. Am. Ceram. Soc.* 60 (1977) 51–54.
- [8] K. Kulikowski, Soft magnetic ferrites — Development or stagnation?, *J. Magn. Magn. Mater.* 41 (1984) 56–62.
- [9] P. Ravindranathan, K.C. Patil, Novel solid solution precursor method for the preparation of ultrafine Ni–Zn ferrites, *J. Mater. Sci.* 22 (1987) 3261–3264.
- [10] T. Abraham, Economics of ceramic magnets, *Am. Ceram. Soc. Bull.* 73 (1994) 62–65.
- [11] P.I. Slick, in *Ferromagnetic Materials*, vol. 2, (ed.) E.P. Wohlforth, North-Holland, Amsterdam, 1980, p. 196.
- [12] B.V. Bhise, M.B. Dongare, S.A. Patil, S.R. Sawant, X-ray infrared and magnetization studies on Mn substituted Ni–Zn ferrites, *J. Mater. Sci. Lett.* 10 (1991) 922–924.
- [13] S.A. Saafan, S.T. Assar, B.M. Moharram, M.K. El Nimr, Comparison study of some structural and magnetic properties of nano-structured and bulk Li–Ni–Zn ferrite samples, *J. Magn. Magn. Mater.* 322 (2010) 628–632.
- [14] X. Lu, G. Liang, Q. Sun, and C. Yang, High-frequency magnetic properties of Ni–Zn ferrite nanoparticles synthesized by a low temperature chemical method, *Mater. Lett.* 65 (2011) 674–676.
- [15] B. Zhou, Z. Liu, X. Wang, Y. Sui, X. Huang, Z. Lu, W. Su, Effect of SiO_2 coating on the magnetic properties of Ni–Zn ferrite, *Physica B: Cond. Matt.* 405 (2010) 374–378.
- [16] S. Rohilla, S. Kumar, P. Aghamkar, S. Sunder, and A. Agarwal, Investigations on structural and magnetic properties of cobalt ferrite/silica nanocomposites prepared by the co-precipitation method, *J. Magn. Magn. Mater.* 323 (2011) 897–902.
- [17] G. A. Sawatzky, F van der Woude, and A. H. Morrish, Mössbauer Study of Several Ferrimagnetic Spinel, *Phys. Rev.* 187 (1969) 747–757.
- [18] G. A. Pettit and D. W. Forester, Mossbauer study of Co–Zn ferrites, *Phys. Rev. B* 4 (1971)

3912-3923.

- [19] T. Sato, K. Haneda, M. Seki, and T. Iijima, Morphology and magnetic properties of ultrafine ZnFe_2O_4 particles, *Appl. Phys. A: Mater. Science and Processing*. 50 (1990) 13-16.
- [20] D. Hork, B. Rittich, A. Spanov, D. Horak, and A. Spanova, Carboxyl-functionalized magnetic microparticle carrier for isolation and identification of DNA in dairy products, *J. Magn. Magn. Mater.* 311 (2007) 249–254.
- [21] J. Prodelalova, B. Rittich, A. Spanova, K. Petrova, and M. J. Benes, Isolation of genomic DNA using magnetic cobalt ferrite and silica particles, *J. Chromatography A1056* (2004) 43-48.
- [22] Y. Koseoglu, M. Bay, M. Tan, A. Baykal, H. Sozeri, R. Topkaya, and N. Akdogan, Magnetic and dielectric properties of $\text{Mn}_{0.2}\text{Ni}_{0.8}\text{Fe}_2\text{O}_4$ nanoparticles synthesized by PEG-assisted hydrothermal method, *J. Nanoparticle Res.* 13 (2010) 2235-2244.
- [23] G. Vaidyanathan, S. Sendhilnathan, Characterization of $\text{Co}_{1-x}\text{Zn}_x\text{Fe}_2\text{O}_4$ nanoparticles synthesized by co-precipitation method, *Physica B: Condensed Matter* 403 (2008) 2157-2167.
- [24] I. Sharifi, H. Shokrollahi, S. Amiri, Ferrite-based magnetic nanofluids used in hyperthermia applications, *J. Magn. Magn. Mater.* 324 (2012) 903-915.
- [25] V.S.S.P. Gaikwad, H.S. Potdar, V. Ravi, and S.R. Dhage, Co-precipitation method for the preparation of nanocrystalline ferroelectric $\text{SrBi}_2\text{Nb}_2\text{O}_9$ ceramics *J. Electroceramics* 14 (2005) 83-87.
- [26] Hua Su, Xiaoli Tang, Huaiwu Zhang, Yulan Jing, and Zhiyong Zhong, Effects of Nb_2O_5 on DC-Bias-Superposition Characteristic of the Low-Temperature-Fired NiCuZn Ferrites, *IEEE Trans. Magn.* 49 (2013) 4222-4225.
- [27] Shuoqing Yan, Li Dong, Zhongyan Chen, Xian Wang, Zekun Feng, Shuoqing Yan, Li Dong, Zhongyan Chen, Xian Wang, Zekun Feng, The effect of the microstructure on the DC-bias superposition characteristic of NiCuZn ferrite, *J. Magn. Magn. Mater.* 353 (2014) 47-50.
- [28] H. Su, H. Zhang, X. Tang, B. Liu, Z. Zhong, Effects of Co- substitution on DC-bias-superposition characteristic of the NiCuZn ferrites, *Physica B* 405 (18) (2010) 4006-4009.
- [29] Hai-Bo Wang, Jin Hong Liu, Wen Fing Li, Jian-Bo Wang, Li Wang, Li-Jing Song, Shi-Jun Yuan, Fa-Shen Li, and F.S. Li, Structural, dynamic magnetic and dielectric properties of $\text{Ni}_{0.15}\text{Cu}_{0.2}\text{Zn}_{0.65}\text{Fe}_2\text{O}_4$ ferrite produced by NaOH co-precipitation method, *J. Alloys Compd.* 461 (1-2) (2008) 373-377.
- [30] Hua Su, Xiaoli Tang, Huaiwu Zhang, Yulan Jing, Zhiyong Zhong, Low-temperature-fired NiCuZn ferrites with BBSZ glass, *J. Magn. Magn. Mater.* 323(5) (2011) 592-595.
- [31] J. Murbe and J. Topfer, Ni-Cu-Zn Ferrites for low temperature firing: II. Effects of powder morphology and Bi_2O_3 addition on microstructure and permeability, *J. Electroceramics* 16 (2006) 199-205.

- [32] T. Krishnaveni, B. Rajini. Kanth, V. Seetha Rama Raju and S. R. Murthy, Fabrication of multilayer chip inductors using Ni–Cu–Zn ferrites, *J. Alloys Compd.* 414 (1-2) (2006) 282-286.
- [33] O. F. Caltun, L. Spinu, A. Stancu, L. D. Thung, and W. Zhou, Study of the microstructure and of the permeability spectra of Ni–Zn–Cu ferrites, *J. Magn. Magn. Mater.* 242 (2002) 160-162.
- [34] Wei-Chih Hsu, S.C Chen, P.C Kuo, C.T Lie, W.S Tsai, Preparation of NiCuZn ferrite nanoparticles from chemical co-precipitation method and the magnetic properties after sintering, *Mater. Sci. Engg. B.* 111 (2004) 142-149.
- [35] Yao Li, Jiupeng Zhao, Jiecai Han, Xiaodong He, Combustion synthesis and characterization of NiCuZn ferrite powders, *Mater. Res. Bull.* 40 (2005) 981-989.
- [36] P. K. Roy and J. Bera, Effect of Mg substitution on electromagnetic properties of $(\text{Ni}_{0.25}\text{Cu}_{0.20}\text{Zn}_{0.55})\text{Fe}_2\text{O}_4$ ferrite prepared by auto combustion method, *J. Magn. Magn. Mater.* 298 (1) (2006) 38-42.
- [37] Hua Su, Xiaoli Tang, Huaiwu Zhang, Lijun Jia, Zhiyong Zhong, Influences of Fe-deficiency on electromagnetic properties of low-temperature-fired NiCuZn ferrites, *J. Magn. Magn. Mater.* 322(13) (2010) 1779-1783.
- [38] S.H. Hong, J.H. Park, Y.H. Choa, J. Kim, Magnetic properties and sintering characteristics of NiZn (Ag, Cu) ferrite for LTCC applications, *J. Magn. Magn. Mater.* 290-291 (2005) 1559-1562.
- [39] L. Ma, L. Chen, S. Chen, Study on the characteristics and activity of Ni–Cu–Zn ferrite for decomposition of CO_2 , *Mater. Chem. Phys.* 114 (2009) 692-696.
- [40] Hua Su, Huaiwu Zhang, Xiaoli Tang, Yulan Jing, Effects of nanocrystalline ferrite particles on densification and magnetic properties of the NiCuZn ferrites, *J. Mater. Sci.* 42(8) (2007) 2849-2853.
- [41] I.H. Gul, W. Ahmed, A. Maqsood, Electrical and magnetic characterization of nanocrystalline Ni–Zn ferrite synthesis by co-precipitation route, *J. Magn. Magn. Mater.* 320(3–4) (2008) 270–275.
- [42] S. Zahi, M. Hashim, A.R. Daud, Synthesis, magnetic properties and microstructure of Ni–Zn ferrite by sol–gel technique, *Journal of Magnetism and Magnetic Materials* 308(2) (2007) 177–182.
- [43] A. Košak, D. Makovec, A. Žnidaršič A, et al, Preparation of Mn-Zn ferrite with microemulsion technique, *Journal of the European Ceramic Society* 24(6) (2004) 959–962.
- [44] X. Jiao, D. Chen, Y. Hu, Hydrothermal synthesis of nanocrystalline $\text{M}_x(\text{Zn}_{1-x})\text{Fe}_2\text{O}_4$ (M = Ni, Mn, Co; $x = 0.40\text{--}0.60$) powders, *Materials Research Bulletin* 37(9) (2002) 1583–1588.
- [45] A. Takayama, M. Okuya, S. Kaneko, Spray pyrolysis deposition of NiZn ferrite thin films. *Solid State Ionics* 172(1–4) (2004) 257– 260.
- [46] S.Thakur, S.C. Katyal, M. Singh, Structural and magnetic properties of nano nickel–zinc ferrite

synthesized by reverse micelle technique. *Journal of Magnetism and Magnetic Materials* 321(1) (2009) 1–7.

- [47] P.P. Sarangi, S.R. Vadera, M.K. Patra, et al. Synthesis and characterization of pure single phase Ni–Zn ferrite nanopowders by oxalate based precursor method. *Powder Technology* 203(2) (2010) 348–353.
- [48] S. Balaji, K. Kalai Selvan, L. John Berchmans, et al. Combustion synthesis and characterization of Sn^{4+} substituted nanocrystalline NiFe_2O_4 . *Materials Science and Engineering B* 119(2) (2005) 119–124.
- [49] Praveena Kuruva, Uma Maheshwara Singh Rajaputra, Srinath Sanyadanam, Ramana Murthy Sarabu, Effect of microwave sintering on grain size and dielectric properties of barium titanate, *Turkish Journal of Physics* 37 (2013) 312–321.
- [50] K. Praveena, K. Sadhana, S. Srinath, S.R. Murthy, Effect of TiO_2 on electrical and magnetic properties of $\text{Ni}_{0.35}\text{Cu}_{0.12}\text{Zn}_{0.35}\text{Fe}_2\text{O}_4$ synthesized by the microwave–hydrothermal method, *J. Phys. Chem. Solids* 74 (2013) 1329–1335.
- [51] K. Praveena, K. Sadhana, S.R. Murthy, Microwave-hydrothermal synthesis of $\text{Ni}_{0.53}\text{Cu}_{0.12}\text{Zn}_{0.35}\text{Fe}_2\text{O}_4/\text{SiO}_2$ nanocomposites for MLCI, *Integrated Ferroelectrics* 119(1) (2010) 122–134.
- [52] Sadhana Katlakunta, Sher Singh Meena, S. Srinath, M. Bououdina, R. Sandhya, K. Praveena, Improved magnetic properties of Cr^{3+} doped $\text{SrFe}_{12}\text{O}_{19}$ synthesized via microwave hydrothermal route, *Materials Research Bulletin* 63 (2015) 58–66.
- [53] S.T. Aruna, A.S. Mukasyan, Combustion synthesis and nanomaterials, *Current Opinion in Solid State and Materials Science* 12(3–4) (2008) 44–50.
- [54] V.G. Patil, Sagar E. Shirsath, S.D. Morec, S.J. Shukla, and K.M. Jadhav, Effect of zinc substitution on structural and elastic properties of cobalt ferrite, *J. Alloys Compd.* 488 (2009) 199–203.
- [55] S. Kumar, V. Singh, S. Aggarwal, U.K. Mandal, and R.K. Kotnala, Influence of processing methodology on magnetic behavior of multicomponent ferrite nanocrystals, *J. Phys. Chem. C* 114 (2010) 6272–6280.
- [56] Ibrahim Sharifi, and H. Shokrollahi, Nanostructural, magnetic and Mössbauer studies of nanosized $\text{Co}_{1-x}\text{Zn}_x\text{Fe}_2\text{O}_4$ synthesized by co-precipitation, *J. Magn. Magn. Mater.* 324 (2012) 2397–2403.
- [57] A. Navrotsky, and O.J. Kleppa, Thermodynamics of Formation of Simple Spinel, *J. Inorg. Nucl. Chem.* 30 (1968) 479–498.
- [58] C. Upadhyay, H.C. Verma, S. Anand, Cation distribution in nanosized Ni–Zn ferrites, *J. Appl. Phys.* 95 (2004) 5746–5751.
- [59] D. Domide, O. Walter, S. Behrens, E. Kaifer, and H.J. Himmel, Synthesis of Heterobimetallic Zn/Co Carbamates: Single-Source Precursors to Nanosized Magnetic Oxides under Mild Conditions, *Eur. J. Inorg. Chem.* 2011(6) (2011) 860–867.

- [60] M. Sertkol, Y. Koseoglu, A. Baykal, H. Kavas, A. Bozkurt, and M.S. Toprak, Cation distribution and magnetic properties of Zn doped NiFe_2O_4 nanoparticles synthesized by PEG-assisted hydrothermal route, *J. Alloys Compd.* 479 (2009) 49-55.
- [61] R.C. Kambale, P.A. Shaikh, S.S. Kamble, and Y.D. Kolekar, Effect of cobalt substitution on structural, magnetic and electric properties of nickel ferrite, *J. Alloys Compd.* 478 (2009) 599-603.
- [62] A. Baykal, N. Kasapoglu, Y. Koseoglu, A.C. Basaran, H. Kavas, and M.S. Toprak, Microwave- induced combustion synthesis and characterization of $\text{Ni}_x\text{Co}_{1-x}\text{Fe}_2\text{O}_4$ nanocrystals ($x = 0.0, 0.4, 0.6, 0.8, 1.0$), *Cent. Eur. J. Chem.* 6 (2008) 125-130.
- [63] Y. Koseoglu, A. Baykal, M.S. Toprak, F. Gozuak, A.C. Basaran, and B. Aktas, Synthesis and characterization of ZnFe_2O_4 magnetic nanoparticles via a PEG-assisted route, *J. Alloy Compd.* 462 (2008) 209-213.
- [64] A. Baykal, N. Kasapoglu, Y. Koseoglu, M.S. Toprak, H. Bayrakdar, CTAB-assisted hydrothermal synthesis of NiFe_2O_4 and its magnetic characterization, *J. Alloys Compd.* 464 (2008) 514-518.
- [65] M. Sertkol, Y. Koseoglu, A. Baykal, H. Kavas, A. Bozkurt, and M.S. Toprak, Microwave synthesis and characterization of Zn-doped nickel ferrite nanoparticles *J. Alloys Compd.* 486 (2009) 325-329.
- [66] C. Upadhyay, H.C. Verma, S. Anand, Cation distribution in nanosized Ni–Zn ferrites, *J. Appl. Phys.* 95 (2004) 5746-5751.
- [67] L. Neel, C. R. Acad. Sci. Paris, Aimantation à saturation des ferrites mixtes de nickel et de zinc, 230 (1950) 375-377.
- [68] G. Vaidyanathan, S. Sendhilnathan, R. Arulmurugan, Structural and magnetic properties of $\text{Co}_{1-x}\text{Zn}_x\text{Fe}_2\text{O}_4$ nanoparticles by co-precipitation method, *J. Magn. Magn. Mater.* 313(2) (2007) 293-299.
- [69] Misbah Ul Islam, Mazhar Uddin Rana, Tahir Abbas, Study of magnetic interactions in Co–Zn–Fe–O system, *Mater. Chem. Phys.* 57 (1998) 190-193.
- [70] Y. Yafet, and C. Kittel, Antiferromagnetic Arrangements in Ferrites, *Phys. Rev.* 87 (2) (1952) 290-294.
- [71] A.K.M. Akther Hossain, and M.L. Rahman, Enhancement of microstructure and initial permeability due to Cu substitution in $\text{Ni}_{0.50-x}\text{Cu}_x\text{Zn}_{0.50}\text{Fe}_2\text{O}_4$ ferrites, *J. Magn. Magn. Mater.* 323(15) (2011) 1954-1962.
- [72] D.S. Birajdar, D.R. Mane, S.S. More, V.B. Kawade, and K.M. Jadhav, Structural and magnetic properties of $\text{Zn}_x\text{Cu}_{1.4-x}\text{Mn}_{0.4}\text{Fe}_{1.2}\text{O}_4$ ferrites, *Mater. Lett.* 59 (24-25) (2005) 2981-2985.
- [73] M.F. Hansen, and S. Mørup, Estimation of blocking temperatures from ZFC/FC curves *J. Magn. Magn. Mater.* 203 (1999) 214-216.
- [74] A. Franco Jr. and F.C. Silva, High temperature magnetic properties of cobalt ferrite

nanoparticles, Appl. Phys. Lett. 96 (17) (2010) 172505–172508.

- [75] B. Martinez, X. Obradors, L. Balcells, A. Rouanet, and C. Monty, Low Temperature Surface Spin-Glass Transition in γ -Fe₂O₃ Nanoparticles, Phys. Rev. Lett. 80(1) (1998) 181-184.
- [76] Y. Koseoglu, F. Alan, M. Tan, R. Yilgin, and M. Ozturk, Low Temperature Hydrothermal Synthesis and Characterization of Mn-Doped Cobalt Ferrite Nanoparticles, Ceram. Int. 38 (2012) 3625-363.
- [77] Y. Melikhov, J.E. Snyder, D.C. Jiles, A.P. Ring, J.A. Paulsen, C.C.H. Lo, and K.W. Dennis, Temperature dependence of magnetic anisotropy in Mn-substituted cobalt ferrite, J. Appl. Phys. 99 (2006) 08R102-3.
- [78] J.H. Fendler, Nanoparticles and Nanostructured Films, Wiley, New York, 1998, p. 81.
- [79] E.C. Stoner, and E.P. Wohlfarth, A Mechanism of Magnetic Hysteresis in Heterogeneous Alloys, Philosophical Transactions of the Royal Society of London. Series A. Mathematical and Physical Sciences, 240(826) (1948) 599-642.
- [80] L. Victoria, D.C. Clero-del, and C. Rinaldi, Synthesis and magnetic characterization of cobalt-substituted ferrite (Co_xFe_{3-x}O₄) nanoparticles, J. Magn. Magn. Mater. 314 (1) (2007) 60-67.
- [81] S. Ammar, A. Helfen, N. Jouini, F. Fievet, I. Rosenman, F. Villain, P. Molinie, and M. Danot, Magnetic properties of ultrafine cobalt ferrite particles synthesized by hydrolysis in a polyol medium, J. Mater. Chem. (Royal Society of Chemistry, UK) 11 (2001) 186-192.
- [82] R.H. Kodama, Magnetic nanoparticles, J. Magn. Magn. Mater. 200 (1999) 359-372.
- [83] G. Hadjipanayis, D.J. Sellmyer, and B. Brandt, Rare-earth-rich metallic glasses. I. Magnetic hysteresis, Phys. Rev. B 23(7) (1981) 3349-3354.
- [84] M. Tachiki, Origin of the magnetic anisotropy energy of cobalt ferrite, Progress of Theoretical Physics 23(6) (1960) 1055-1072.
- [85] S.S. Jadhav, S.E. Shirsath, S.M. Patange, and K.M. Jadhav, Effect of Zn substitution on magnetic properties of nanocrystalline cobalt ferrite, J. Appl. Phys. 108 (2010) 093920-6.
- [86] J. Gao, W. Zhang, P. Huang, B. Zhang, X. Zhang, and B. Xu, Intracellular spatial control of fluorescent magnetic nanoparticles, J. Am. Chem. Soc. 130(12) (2008) 3710-3711.
- [87] S. Pal, S. Chandra, M.H. Phan, P. Mukherjee, and H. Srikanth, Carbon nanostraws: nanotubes filled with super-paramagnetic nanoparticles, Nanotechnology IOP 20 (48), (2009) 485604 (7 pages).
- [88] K. Bhattacharjee, C. K. Ghosh, M. K. Mitra, G. C. Das, S. Mukherjee, Kalyan Kumar Chattopadhyay, Novel synthesis of Ni_xZn_{1-x}Fe₂O₄ (0≤x≤1) nanoparticles and their dielectric properties, J. Nanoparticle Res. 13 (2011) 739-750.

- [89] K. H. Wu, T. H. Ting, M. C. Lia and W. D. Ho, Sol-gel auto-combustion synthesis of SiO₂-doped NiZn ferrite by using various fuels, *J. Magn. Magn. Mater.* 298 (2006) 25-32.
- [90] H. Chyi Ching, W. Tsung Yung, W. Jun, T. Jih Sheng, Development of a novel combustion synthesis method for synthesizing of ceramic oxide powders, *Mater. Sci. Eng. B* 111 (2004) 49-56.
- [91] J. Livage, C. Sanchez, M. Henry and S. Doeuff, The chemistry of the sol-gel process, *Solid State Ionics* 32/33 (1989) 633-638.
- [92] C. J. Brinker and G. W. Scherer, *Sol-Gel Science*, Academic Press, San Diego, 1990, pp. 21-78.
- [93] M. Epifani, E. Melissano, G. Pace, M. Schioppa, Precursors for the combustion synthesis of metal oxides from the sol-gel processing of metal complexes, *J. Eur. Ceram. Soc.* 27 (2007) 115-123.
- [94] C.A. Jakobson (ed.), *Encyclopedia of Chemical Reactions*, Reinhold Publishing, New York, (1953), vol. V, pp. 175.
- [95] X. Tang, H. Zhang, H. Su, Z. Zhong, and F. Bai, Influence of Microstructure on the DC-Bias-Superposition Characteristics of NiZn Ferrites, *IEEE Trans. Magn.* 47 (2011) 4332-4335.
- [96] www.fair-rite.com/newfair/pdf/Directcurrent.pdf for document 'The Effect of Direct Current on the Inductance of a Ferrite Core', Fair-Rite Product's Catalog, Part Data Sheet, 9477016002, Printed: 2010-11-09.
- [97] Sea-Fue Wang, Yuh-Ruey Wang, Thomas C.K Yang, Po-Jeng Wang, Chun-An Lu, Densification and properties of fluxed sintered NiCuZn ferrites, *J. Magn. Magn. Mater.* 217(1-3) (2000) 35-43.